공학박사 학위논문

Thermomechanical constitutive modelling of rate-dependent and anisotropic shape memory polymers

속도 의존성 및 이방성을 갖는 형상기억고분자의

열기계적 모델링

2023 년 2월

서울대학교 대학원

재료공학부

김 진 수

Thermomechanical constitutive modelling of rate-dependent and anisotropic shape memory polymers

Advisor : Woong-Ryeol Yu

by

Jinsu Kim

2023

Department of Materials Science and Engineering Graduated School Seoul National University

Thermomechanical constitutive modelling of rate-dependent and anisotropic shape memory polymers

속도 의존성 및 이방성을 갖는 형상기억고분자의 열기계적 모델링

지도 교수 유 웅 열

이 논문을 공학박사 학위논문으로 제출함

2022 년 12 월

서울대학교 대학원

재료공학부

김 진 수

김진수의 공학박사 학위논문을 인준함

2022 년 12 월

위 원 장	안철희	(인)
부위원장	유웅열	(인)
위 원	이명규	(인)
위 원	나원진	(인)
위 원	홍석빈	(인)

Abstract

Shape-memory polymers (SMPs) are a class of smart materials that can recover a permanent shape from a programmed temporary shape in response to an external stimulus, such as temperature, electricity, light, or humidity. Furthermore, the introduction of liquid crystals (mesogen) into shape memory polymers (LCE, Liquid crystal elastomers) reveals new characteristics of SMP according to its direction. One of the remarkable features of LCEs is that the orientation of mesogen changes with external force and temperature. Using these properties, ordered LCEs can change reversibly dimensions under low or no external stress through phase transitions. For the successful design of devices employing SMPs and LCEs, constitutive models have been developed to predict shape memory and recovery capability of SMPs and LCEs under various conditions. In this study, a temperature-rate dependent and anisotropic 3D constitutive model is developed for SMPs and LCEs based on a two-phase model consisting of rubbery and glassy phases.

To describe the effect of temperature-rate on SMPs, the variation of the volume fraction of each phase that depends on the temperature is considered

at different temperature rates. In addition, the temperature-rate dependent thermal strain is added to the two-phase model. Poynting–Thomson model and Arruda-Boyce model are used for the rubbery phase and the glassy phase, respectively. To describe the effect of temperature-rate on SMPs, the volume fraction of each phase is considered from the normalized storage modulus curves obtained under different thermal rate conditions. In addition, the temperature-rate dependent thermal strain is added to the two-phase model in series. The material parameters of SMPs for the 3D constitutive equation are determined by measuring uniaxial tensile and creep behavior. The constitutive equation is validated by simulating the thermo-mechanical behavior of 1D rectangular slab and a 3D antenna.

Thermomechanical modelling and simulation of Liquid crystal elastomers (LCEs) are challenging because the orientation of mesogens is affected by not only external force but also temperature. In this study, a new approach constitutive model for LCE was developed considering anisotropic properties of mesogen based on the isotropic rate-dependent model. The backbone polymer, a component of LCE, was modeled using the two-phase model. Then, the orientation of mesogen according to temperature and external force was defined through the WAXS experiment. Based on the experimental

results, the direction vector of mesogen was newly defined as a function of temperature and deformation. It is assumed that the mesogen behaves linearly elastically in the local coordinate, and tensor transformation is used to define the stress according to the temperature and deformation of the mesogen in the global coordinate. Last, the curing strain is adopted to describe the driving force which play a role of the formation of a monodomain of liquid crystals below T_i. The anisotropic constitutive model is validated by simulating the thermo-mechanical behavior of LCE under various boundary conditions.

Contents

3 Constitutive modelling of anisotropic Liquid crystal elastomers

List of Figures

polymer (SMP). (d, e) Procedure for folding and recovery. (a–c) Experimental set-up for the deployable antenna: (a) folding device; (b) SMP specimen mounted on the folding device inside an environmental chamber; (c) set-up for recording the deployment behavior.

Figure 21 Experimental and simulation results of the uniaxial thermomechanical cycling test. (a) Engineering strain as a function of time (solid and dash–dot lines represent the simulation and experimental results, respectively), (b) input temperature, (c) volume fraction of the glassy phase as a function of time, (d) thermal strain from the thermal deformation gradient as a function of time, and (e) three-dimensional shape changes under the temperature-rate condition of 5°C/min. The color indicates the nominal strain.

Figure 22 Stress evolution during a uniaxial thermomechanical cycling test. (a) Engineering stress as a function of time (solid and dash–dot lines represent the simulation and experimental results, respectively) and (b) stress distribution in the geometry under the temperature rate condition of 5°C/min. Solid and dash–dot lines represent simulation and experimental results, respectively. The color indicates the nominal stress.

Figure 23 Experimental and modeling results for the self-deployable antenna tests. (a) Input temperature, (b) change in antenna angle as a function of time under different temperature-rate conditions (solid and dash–dot lines represent the simulation and experimental results, respectively), (c–d) shape change under the temperature-rate condition of 5°C/min, (c) experimental images, and (d) simulation results. Solid and dash–dot lines represent the simulation and experimental results, respectively. The color indicates the equivalent strain, i.e.,

$$\varepsilon_{eq} = (2/3)\sqrt{(3/2)(e_{xx}^2 + e_{yy}^2 + e_{zz}^2) + (3/4)(\gamma_{xy}^2 + \gamma_{yz}^2 + \gamma_{zx}^2)}\ ,$$ where e is the

deviatoric strain and γ is the shear strain.

Figure 24 Chemical structure of monomers to produce main-chain LCE in this study. Mesogen monomer (RM257), Linear chain extender for linking mesogens with dithiol functional end group (PDT for exp1 and EDDT for exp2) and Crosslinking monomer with tetrathiol functional end group (PETMP) polymerized via Michael addition.

Figure 25 Dynamic mechanical analysis results of the LCE

1. Introduction

1.1. Shape memory polymers (SMPs) and Liquid crystal elastomers (LCEs)

Shape-memory polymers (SMPs) are a class of smart materials that can recover a permanent shape from a programmed temporary shape in response to an external stimulus, such as temperature, electricity, light, or humidity. Thermoresponsive SMPs have been extensively investigated by manipulating their shape near the transition temperature (T_g). Shape memory can be initiated by deforming the material above its T_g, followed by cooling below the T_g while maintaining the constraint. The programmed temporary shape is obtained after removing the constraint, and the original shape is recovered upon heating above the T_g. Thermally activated SMPs are used in applications such as aerospace, flexible electronics, and biomedical devices due to their ease of processing, and durable and reliable shape-memory effects obtainable even with large deformations [1-3].
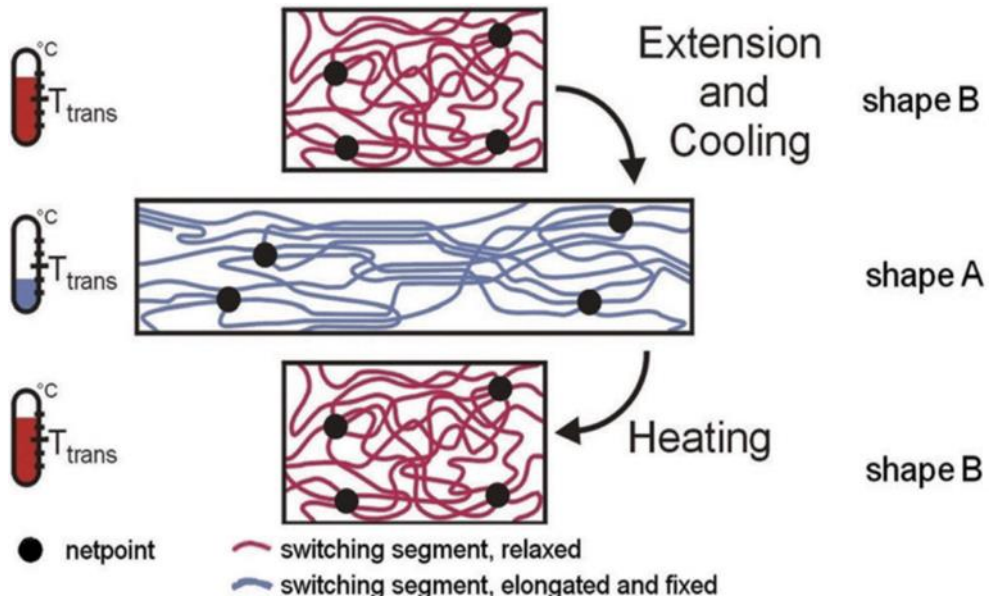
Figure 1 Transition of phases of SMP at shape memory cycle. The shape B in figure shows rubbery phase at high temperature (above T_g) and shape A shows glassy phase (below T_g) after deformation. Gained from reference [4].

In addition, the introduction of liquid crystals (mesogen) into elastomers (LCE, Liquid crystal elastomers) reveals new characteristics of SMP according to its direction [5-12]. Liquid Crystal Elastomer (LCE) refers to a polymer in which rigid liquid crystal molecules called mesogen are weakly crosslinked to a flexible polymer chain. The characteristic of LCE, which has very high elasticity and flexibility due to the crosslinking point, is that the mesogen molecules with directionality and position are arranged according to external stimuli (heat, UV, electric field, magnetic field, moisture, etc.) and behave anisotropic [13]. As the order of the mesogens is

2

disrupted due to external stimuli, the shape of the LCE is reversibly changed according to the direction of the mesogens. Since the arrangement of LCE mesogen affects the actuation performance, work capacity, dissipation, and elastic modulus of LCE, LCE is applied in a wide range of fields such as smart textiles, 3D, 4D printing, soft smart robots, medical materials, and coatings [14-19].
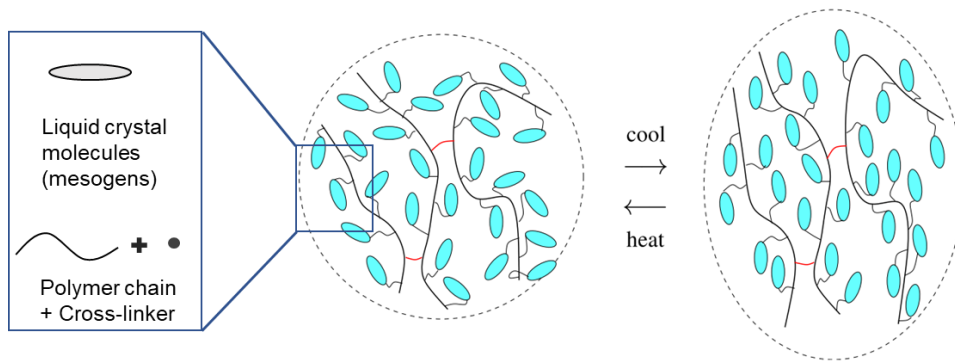
Figure 2 Molecular composition in liquid crystal elastomers and their shape memory mechanism. Gained from the reference [20].
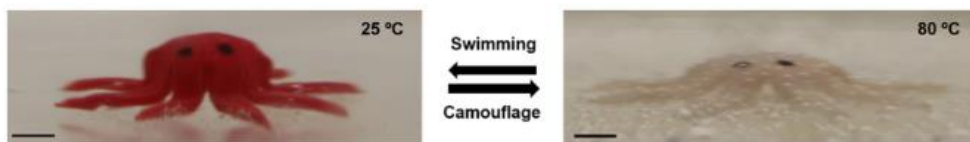
Figure 3 Underwater shape-morphing and color-changing ''octopus'' robot ma de from LCEs. Gained from the reference [21].

1.2. Modelling of SMPs considering rate-dependent behavior

For the successful design of devices employing SMPs, constitutive models have been developed to predict shape memory and recovery capability of SMPs under various thermomechanical conditions. The mechanical properties of SMPs are significantly temperature dependent. At the high temperature well above T_g, the deformation of the SMP in the rubbery state is governed by the conformational entropy change as the interaction between polymer chains becomes negligible. Whereas the change in internal energy due to bond stretching becomes prominent when the SMP in the glassy state deforms at the low temperature far below T_g. From the thermodynamic perspective of entropy and internal energy, continuum phenomenological models have been proposed to describe the thermomechanical behavior of SMPs, without incorporating the dynamics of polymer chains at the molecular level.
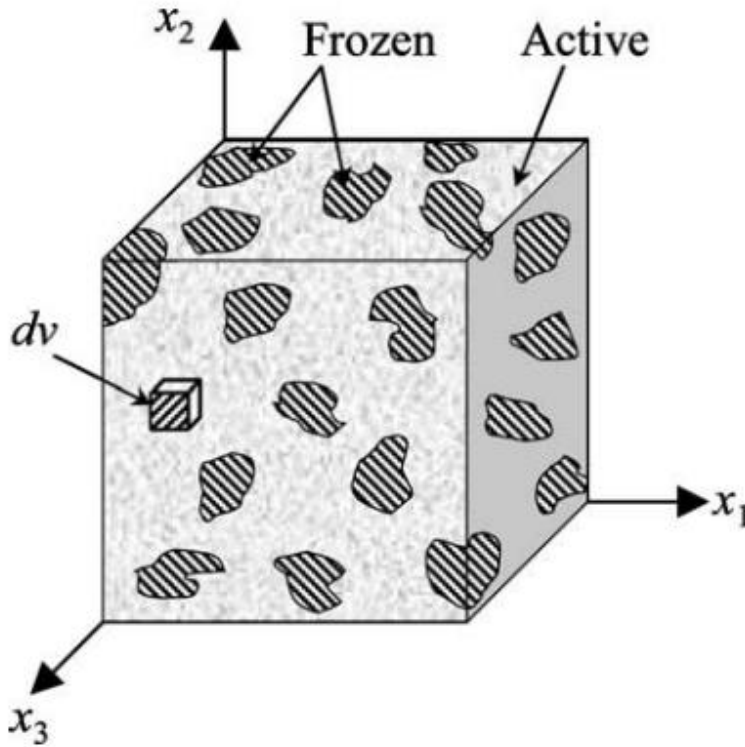
Figure 4 Schematic diagram of the micromechanics foundation of the 3-D s
hape memory polymer constitutive model. Existence of two extreme phases i
n the polymer is assumed. The diagram represents a polymer in the glass tr
ansition state with a predominant active phase. Gained from the reference [2
2].

In the previous models, SMPs are generally considered to be composed of two

phases, a rubbery phase and a glassy phase dominated by entropy and internal energy,

respectively [23-39]. The rubbery phase is expressed as a rheological model in which

springs and dashpots are connected in series [23-27, 32-34] or in parallel [29, 37] to

implement viscoelasticity. The glassy phase is modeled by a single spring element, assuming that all entropic contributions are converted to stored internal energy below T_g [26, 27, 29, 30, 37]. The models of glassy phase are improved by further considering the intermolecular resistance, leading to rate-dependent plastic flow. In these cases, the glassy phase is described as the series connection of a spring and a sliding frictional element to represent viscoplasticity [23-25, 32, 34]. In addition to the two phases, the strain storage concept is utilized to account for the shape memory effect. The shape memory strain (or non-mechanical strain) that stores or releases depending on the temperature, is introduced [27, 29-33, 36, 37, 39].
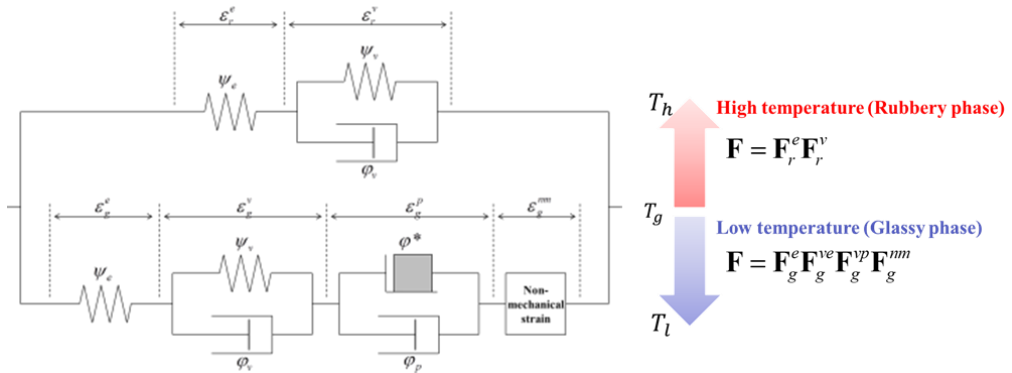
Figure 5 Two-phase phenomenological model for SMPs. Gained from the reference [32]

To reflect temperature dependent viscoelastic behavior of SMPs, the thermal effect is also taken account in various perspective into the previous models mainly categorized as a multi-phase constitutive model and a thermoviscoelastic model. The

common feature of the multi-phase model is that the overall mechanical behavior is predicted by simple rule of mixture type approximations [27, 29-33, 38, 40]. The volume fraction of each phase as function of temperature is experimentally obtained by measuring free strain recovery [27, 38], stress relaxation [32] and storage modulus [29, 31, 40] under temperature sweep from below T_g to above T_g. The thermoviscoelastic model is developed by modifying viscoelastic models. Material parameters are determined as a function of temperature by evaluating dynamic modulus under constant loading frequencies [35, 41]. To increase the accuracy of the existing models, the thermal strain, which is volume expansion or shrinkage due to the temperature change, is added by considering thermal expansion coefficient at constant temperature rate [23-26, 34, 36, 37, 39]. Although the thermomechanical behavior of SMPs can be speculated by the above models, the prediction was deviated for SMPs sensitive to thermal rate. The polymer structure cannot be instantly evolved with a sudden change around T_g, resulting in an out-of-equilibrium state, termed structural relaxation [28]. The previous models are limited to reflect such an effect, causing out-of-equilibrium volume deviation compared with the equilibrium state. For example, the stress overshoot, in which greater stress occurs during constrained recovery than initial stress, cannot be simulated with previous models [42].
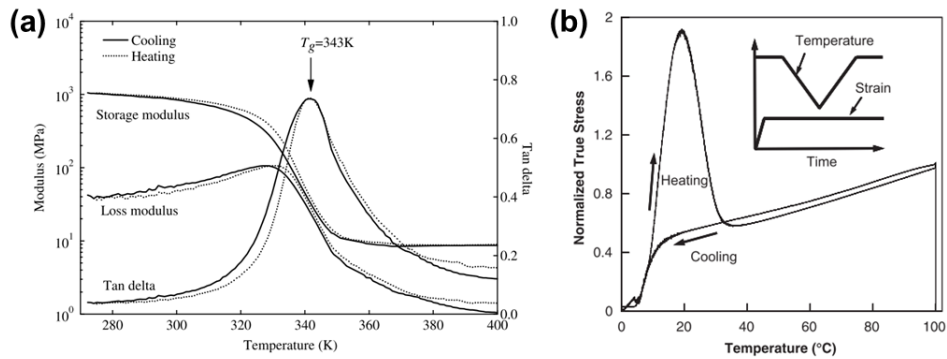
Figure 6 Dynamic mechanical properties of SMPs (a) Variation of storage modulus [27], and (b) Stress–temperature plot during cooling-heating for the constraint condition [31].

1.3. Anisotropic modelling of LCEs

LCE is mainly composed of backbone polymer and mesogen. Backbone polymer shows isotropic mechanical properties like general polymers, but distinct properties based on the glass transition temperature (rubbery properties below T_g, and glassy properties above T_g). Mesogen, another component of LCE, binds to the backbone polymer and shows anisotropic behavior depending on its directionality. The direction of mesogen changes not only by external force, but also by temperature based on a specific temperature (T_i) [43, 44].

8
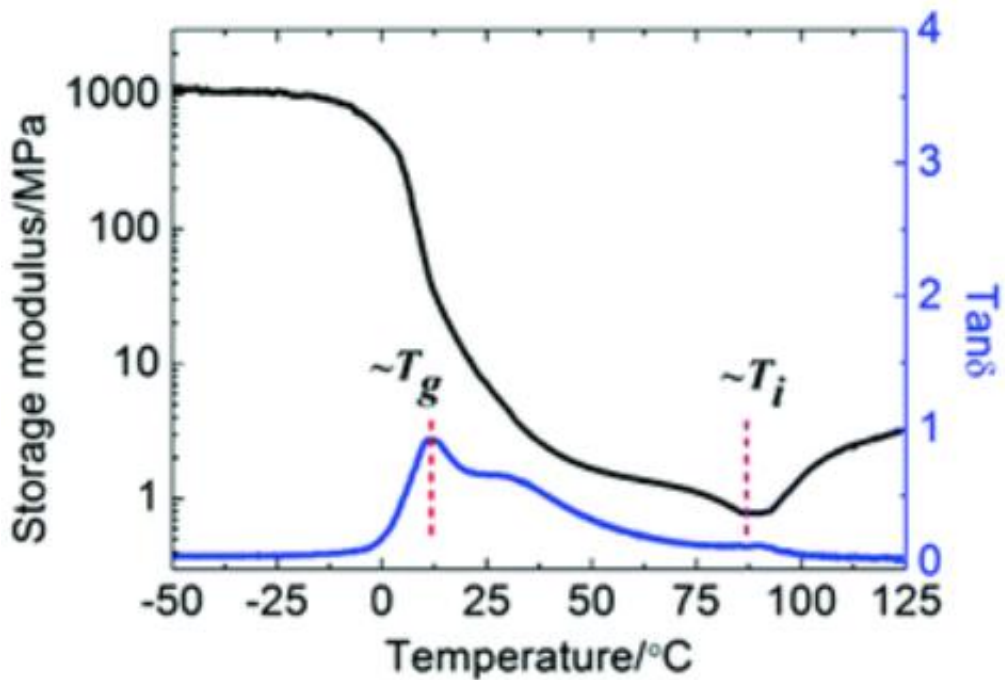
Figure 7 Dynamic behavior of LCEs. Gained from the reference [17]

Deformation of LCE by external force causes the reorientation of mesogen direction along the stretching axis. Due to orientation of the mesogen, the mechanical behavior of LCE is different from that of general isotropic polymers [45-47]. LCE (macroscopically nonaligned polydomain) with randomly arranged mesogens behaves like isotropic material. However, uniaxial stretching of LCE with a randomly disordered director field drives a transition to the monodomain state (Director aligned with the stretching direction). This polydomain-to-monodomain transition occurs in a finite range of stretch at a small constant force. deformed states, respectively), are used in the figure 7 [48]. Before stretching, LCE is opaque because

9

of the strong light scattering of disordered birefringent domains (randomly orientated mesogen). Stretching to the LCE induce the transition from polydomain to monodomain alignment along the stretching axis, and the monodomain alignment is readily confirmed by a fully transparent appearance [49].
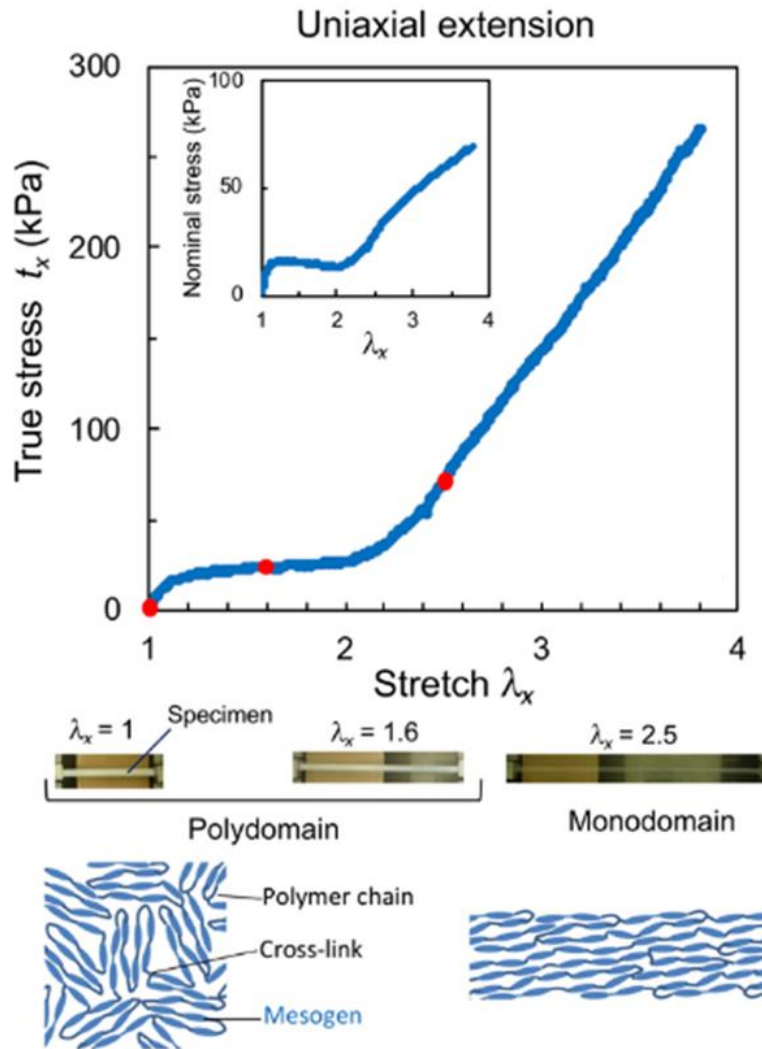
Figure 8 Uniaxial extension to LCE drives polydomain to monodomain state (The initial polydomain is characterized by the turbid appearance reflecting the randomly disordered birefringent domains. The monodomain texture is characterized by the transparent appearance.). The figure is reconstructed from reference [50].

The directionality of mesogen according to temperature changes differently from that of mesogen according to external force. In previous studies, the direction of mesogen according to temperature was experimentally observed [51, 52]. The average direction of mesogen was defined as order parameters $<P_2>=\dfrac{3\cos^2\theta-1}{2}$

and $<P_4>=\dfrac{35\cos^4\theta-30\cos^2\theta+3}{8}$ (θ is the average angle of the mesogen to x-axis), and the direction of nematic LCE (mesogen oriented to certain direction) was observed as the temperature increased. In the nematic state (between 30 and 115 °C), the order parameters maintained [53]. However, the order parameters decrease sharply near the nematic-isotropic transition temperature (T_i). In other words, when the directionality of mesogen exceeds T_i, it goes in a random direction regardless of the original directionality [47, 54].
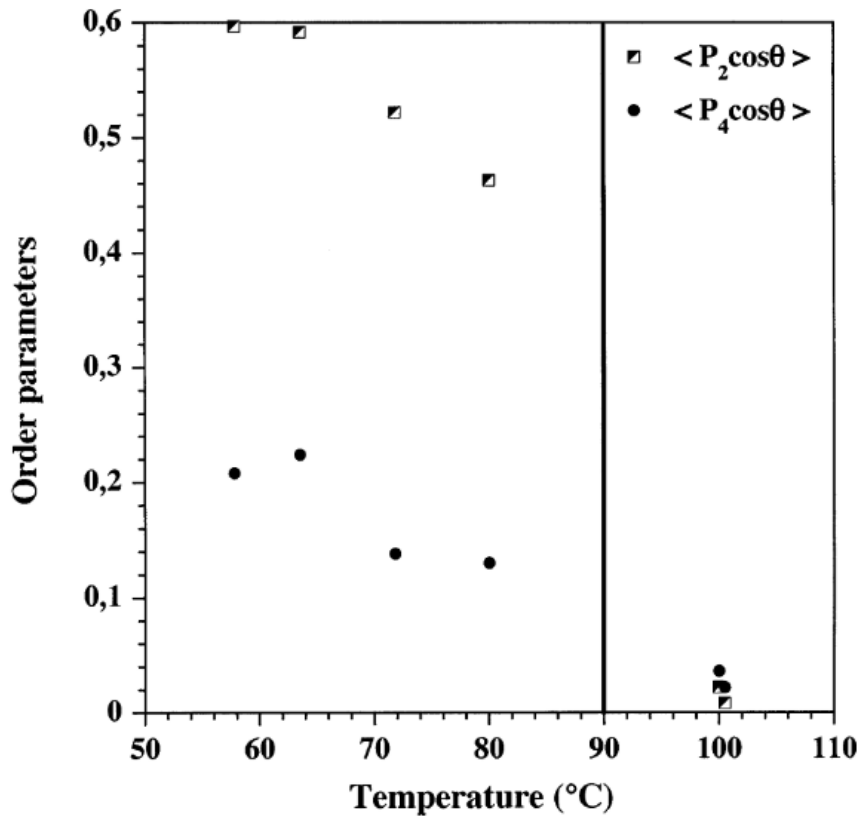
Figure 9 Temperature dependence of the <P2> and <P4> order parameters of the mesogens for the monomer. The vertical line indicates the nematic-isotropic transition. The figure is derived from reference [51].

For identifying the orientation of the mesogen at various conditions, local averages over the distribution of mesogen orientations (Order tensor, $\mathbf{Q}$) have been defined [5]. Order tensor is defined as:

$$Q_{ij} = S(n_i n_j - \frac{1}{3}\delta_{ij})$$ (1)

where n_i are the components of the director **n** in a laboratory (fixed) coordinate system. The scalar quantity S can be obtained by the degree of a local molecular alignment. In the isotropic phase $S = 0$, and $S = 1$ corresponds to a perfect alignment. Using this order tensor system, the constitutive model of LCE have been developed [21, 43, 44, 47, 48, 52, 55-65]. These anisotropic properties of LCE including mesogen were first predicted by de Gennes. The constitutive model is developed using a linear continuum theory in terms of the order tensor of the mesogen groups and the macroscopic, infinitesimal strain tensor. In addition, the model coupled rotations of the mesogenic groups to the elastomeric network strain. This generalized LCE model have been expanded to Brand and Pleiner model which include dynamics as well as external electric and magnetic fields. However, since the scalar order tensor must be defined as a certain value at each condition (figure 9), these models have limitations in explaining the relationship between the morphological tensor of the polymer backbone and the nematic order tensor of the mesogen group.
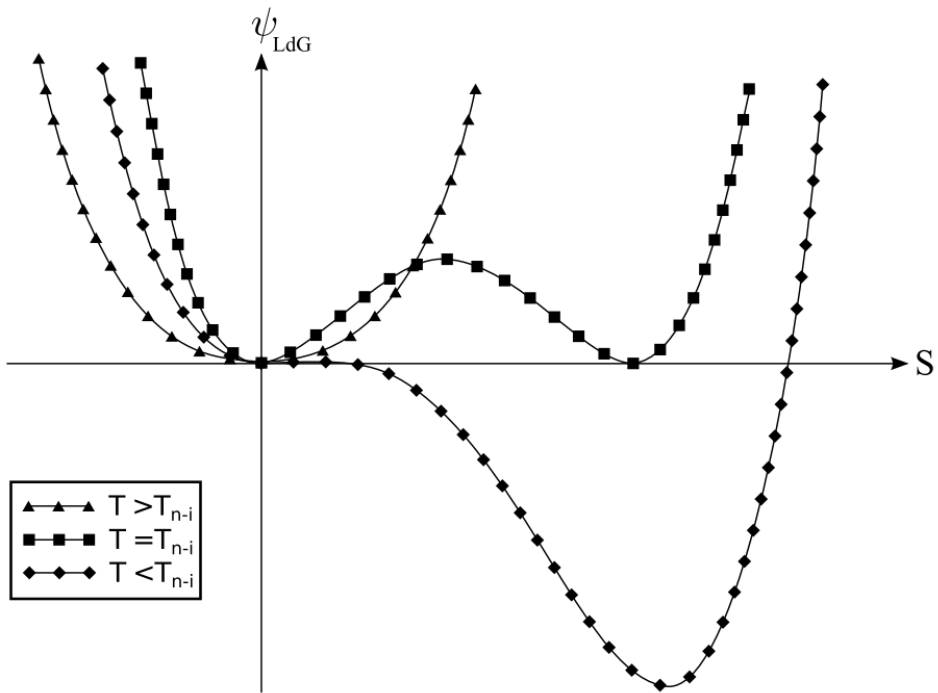
Figure 10 Landau-de-Gennes energy in terms of the nematic scalar order parameter S during the isotropic– nematic phase transition of a uniaxial nematic liquid crystal. Gained from the reference [20].

To overcome these limitations, Carlson et al suggested that order tensors that naturally occur in neoclassical free energy densities and contain unusual combinations of deformation gradients and reference and current shape tensors can be interpreted as nonlinear relative strain tensors. Also, Y. Huo et al developed continuum mechanical theory considering the coupling of the macroscopic deformation and the orientational order for LCEs [20, 65]. In addition to the director

and to their time and space derivatives which are classical in the theory of LCs, the deformation gradient and its time derivative are considered for LCEs. Based on the dissipation principle, the model derived the balance equations of momentum with a Cauchy stress tensor which includes a bulk elastic contribution and an Ericksen–Leslie stress resulting from the change of the orientational order. Although these models can describe the relationship between deformation and direction orientation under various strain rate conditions, the model cannot capture the mechanical behavior of LCEs for continuously different temperature conditions [44, 45, 66-68].
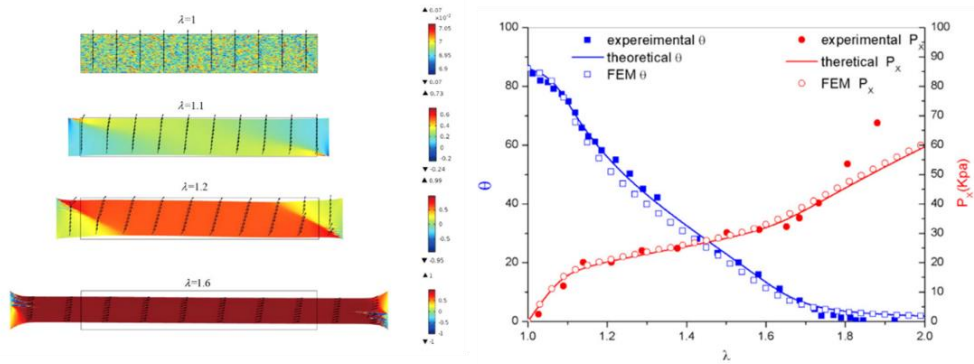
Figure 11 Uniaxial loading with fixed grips of semi-soft LCE samples with $\theta = 86$ °: FEM solutions vs. experiments [44].

1.4. Two-way shape memory behavior of LCEs

LCEs are capable of undergoing reversible transitions between polydomain, monodomain, and isotropic phases. These phases are determined by the organization of mesogens [55, 69-80]. In other words, the molecular orientation governs the anisotropy of macroscopic mechanical response, and monolithic elements composed of these materials can be permanently programmed to exhibit reversible, stimuli-responsive shape transformations.
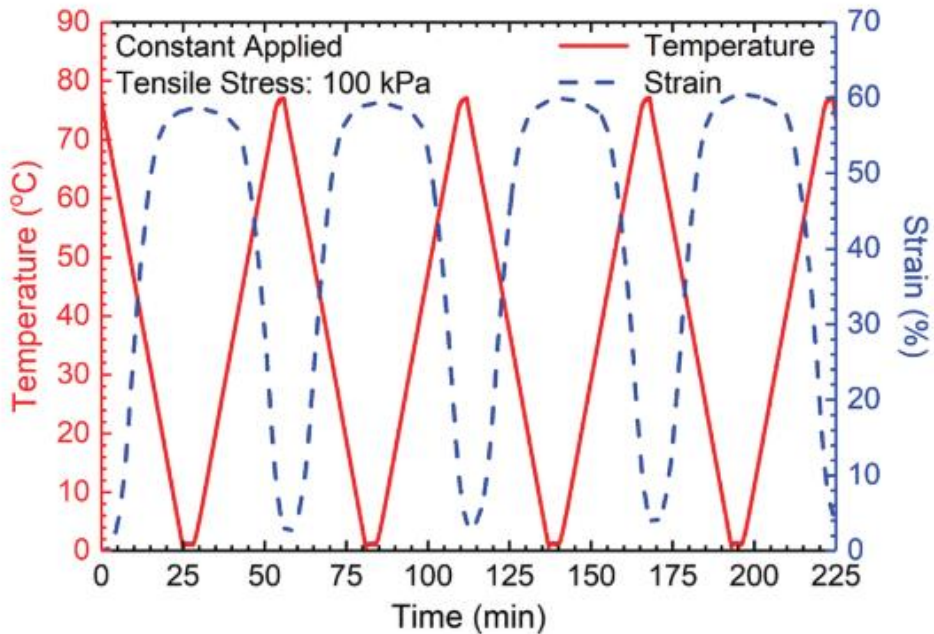
Figure 12 Thermal actuation test with constant stress showing a reversible shape switching strain B60% (dashed blue line). Evolution of corresponding temperature is plotted as solid red line. [54]

For polydomain LCEs, the applied stress drives the formation of the monodomain LCEs at below Ti, which leads to elongation of the material in load direction. Upon heating above Ti, the intermolecular force among the mesogens are disrupted, and the mesogens are randomly distributed in the LCEs. Therefore, the LCE contracts due to entropy elasticity (Figure 12) [54]. Concretely, high temperature above T_i increased with decreased spacer length due to an intense localization of mesogenic monomers in the networks with short spacers. Hence, a higher temperature was required to enable the phase change [74].
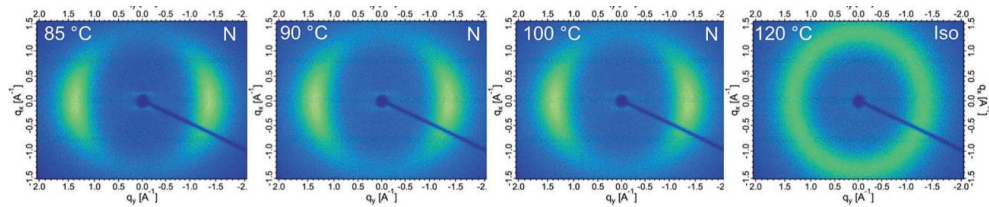
Figure 13 Temperature-controlled WAXS analysis of the LCE system using the C9 spacer. Diffraction patterns reveal the transition from a smectic C to nematic orientation when heated above 80 1C, while a nematic to isotropic transition occurs when heated above 100 1C. All images were taken under 100% engineering strain. Gained from the reference [74].

This is achieved by the formation of a semicrystalline structure with variable re-crystallization rates. Other researchers have studied the increased potential for LCEs using these driving force, achieved by cycling the sample to align the mesogens. Enhancing the stiffness without compromising the strain actuation in inherently

weak materials may lead to a new paradigm of designing the next generation of LCE actuators, which is possible by engineering the microstructure of the LCE networks. However, In the case of monodomain LCE, mesogen alignment is maintained by UV curing without constant stress. To describe the driving force, a new concept of the model is needed.
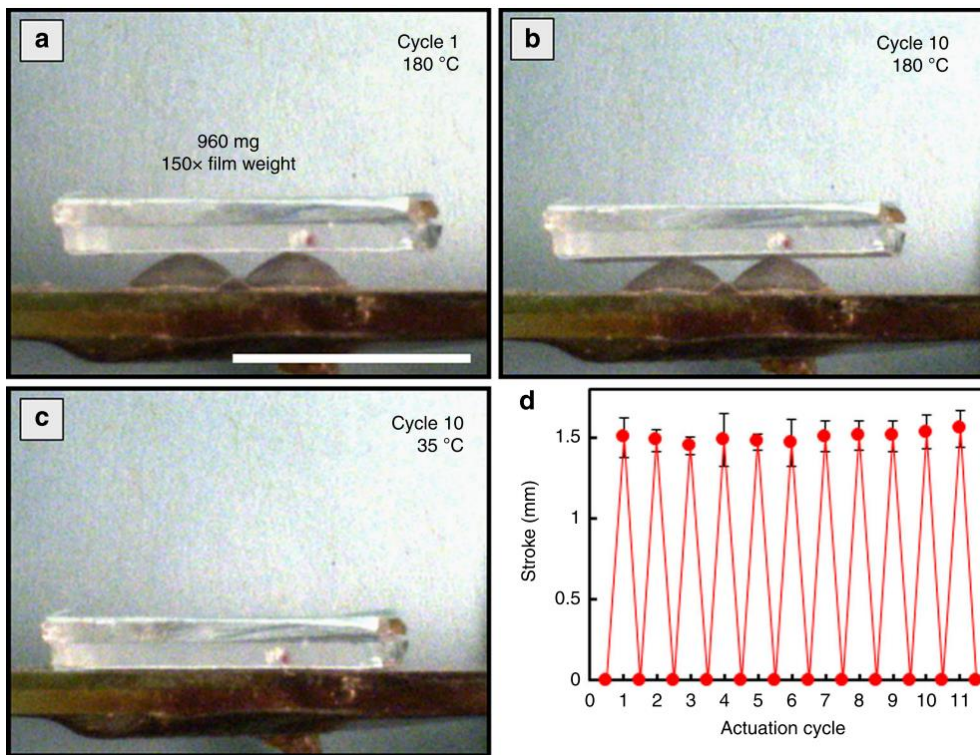
Figure 14 Actuation cycles. Four layer LCE laminate composed of layers with 2×2 array of +1 defects. Scale bar is 1 cm. Deformation of the four layer LCE laminate under 960 mg load was monitored a after 1 cycle, b 10 cycles (heating step), and c 10 cycles (cooling to 35 °C). d Stroke vs thermal cycle for 11 actuation cycles. Error bar is statistical accuracy of measurement [77]

1 8

1.5. Research objective: Rate-dependent and anisotropic constitutive equation of SMP

In this study, a temperature-rate dependent 3D constitutive model is developed for SMPs based on a two-phase model consisting of rubbery and glassy phases. Poynting–Thomson model and Arruda-Boyce model are used for the rubbery phase and the glassy phase, respectively. To describe the effect of temperature-rate on SMPs, the volume fraction of each phase is considered from the normalized storage modulus curves obtained under different thermal rate conditions. In addition, the temperature-rate dependent thermal strain is added to the two-phase model in series. The material parameters of SMPs for the 3D constitutive equation are determined by measuring uniaxial tensile and creep behavior. The constitutive equation is validated by simulating the thermo-mechanical behavior of 1D rectangular slab and a 3D antenna.

Based on the two-phase isotropic rate-dependent model, a new approach constitutive model for LCE was developed considering anisotropic properties of mesogen. The backbone polymer, a component of LCE, was modeled using the two-phase model. Then, the orientation of mesogen according to temperature and external force was defined through the WAXS experiment. Based on the experimental results, the direction vector of mesogen was newly defined as a function of temperature and deformation. It is assumed that the mesogen behaves linearly elastically in the local

coordinate, and tensor transformation is used to define the stress according to the temperature and deformation of the mesogen in the global coordinate. The anisotropic constitutive model is validated by simulating the thermo-mechanical behavior of LCE under various boundary conditions.

2. Constitutive modelling of SMPs considering their non-equilibrium states

2.1. Three-dimensional constitutive model of SMP

2.1.1 Derivation of the constitutive equation

A constitutive model is developed for mathematical description of thermo-mechanical behavior of SMPs. (see). Two parallel phase elements, corresponding to rubbery and glassy phases, and a thermal strain element are connected in serial. The rubbery phase is described by the parallel connection of a hyperelastic Mooney-Rivlin spring and a viscoelastic spring–dashpot element [32]. The glassy phase consists of a linear elastic spring, a viscoplastic element and a shape memory strain (non-mechanical strain) element [32, 81]. The thermal deformation gradient tensor is used to define the thermal strain ($\varepsilon_{thermal}$).
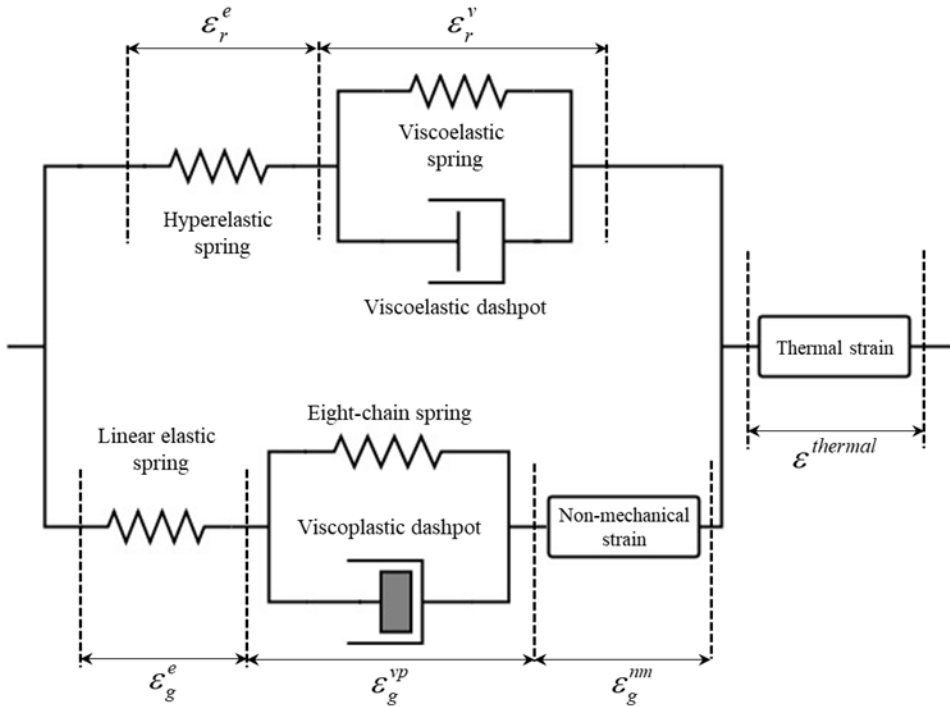
Figure 15 Constitutive model for shape-memory polymers.

The total deformation gradient ($\mathbf{F}_{total}$) was multiplicatively decomposed into mechanical ($\mathbf{F}_{mechanical}$) and thermal deformation ($\mathbf{F}_{thermal}$) gradients (Equation (1)). The mechanical deformation gradient was further decomposed into elastic and other deformation gradients (Equation (2)) [82], as follows:

$$\mathbf{F}_{total} = \mathbf{F}_{mechanical}\mathbf{F}_{thermal} \tag{1}$$

$$\mathbf{F}_{mechanical} = \mathbf{F}_r^h\mathbf{F}_r^v = \mathbf{F}_g^e\mathbf{F}_g^{vp}\mathbf{F}_g^{nm} \tag{2}$$

where superscripts *h*, *v*, e, *vp*, and *nm* represent the hyperelastic spring, viscoelastic component (parallel connection of a hyperelastic spring and dashpot), linear elastic spring, viscoplastic component and shape-memory strain element, respectively. Subscripts *r* and *g* represent the rubbery and glassy phases, respectively.

Using the deformation gradient of each phase, the second Piola-Kirchhoff stresses $\mathbf{S}_r$ and $\mathbf{S}_g$ can be calculated. The second Piola-Kirchhoff stress of the rubbery phase, $\mathbf{S}_r$, is obtained by the following equation [32]:

$$
\begin{aligned}
\mathbf{S}_r &= 2\frac{\partial \psi_r^e}{\partial \mathbf{C}} \\
&= 2\frac{\partial \psi_r^e}{\partial I_r^e}\frac{\partial I_r^e}{\partial \mathbf{C}} + 2\frac{\partial \psi_r^e}{\partial II_r^e}\frac{\partial II_r^e}{\partial \mathbf{C}} + 2\frac{\partial \psi_r^e}{\partial III_r^e}\frac{\partial III_r^e}{\partial \mathbf{C}} \\
&= 2\left(J_r^e\right)^{-2/3}\left[\left(C_{10,r}^e + \bar{I}_r^e C_{10,r}^e\right)\mathbf{I} - \left(J_r^e\right)^{-2/3}C_{01,r}^e\left(\mathbf{C}_r^v\right)^{-1}\mathbf{C}\right]\left(\mathbf{C}_r^v\right)^{-1} \\
&\quad + 2\left\{-\frac{1}{3}\left(\bar{I}_r^e C_{10,r}^e + 2\overline{II}_r^e C_{01,r}^e\right) + \frac{1}{2}\kappa_r^e J_r^e\left(J_r^e - 1\right)\right\}\mathbf{C}^{-T}
\end{aligned} \tag{3}
$$

where I_r^e, II_r^e, and III_r^e are the first, second, and third invariants of the right

2 3

stretch tensor $\mathbf{C}_r^e$ and $\bar{I}_r^e$ and $\bar{II}_r^e$ are the incompressible invariants of I_r^e and II_r^e, respectively. The constants $C_{10,r}^e$, $C_{01,r}^e$, $C_{10,r}^v$, and $C_{01,r}^v$ are the hyperelastic spring constants for each spring element and J_r^e represents the Jacobian function for $\mathbf{C}_r^e$. The Cauchy stress of the glassy phase, $\mathbf{T}_g^e$, was calculated using the following equation:

$$\mathbf{T}_g^e = \frac{1}{\det[\mathbf{F}_g^e]}[\Lambda tr(\mathbf{h})\mathbf{I} + 2G\mathbf{h}]$$

(4)

where $\mathbf{F}_g^e$, $\mathbf{h}$, and $\mathbf{I}$ are deformation gradient of the linear elastic spring, Hencky strain, and identity tensor. Λ and G are material parameters of the Arruda-Boyce model [81]. The Cauchy stress of the glassy phase can be converted to the second Piola-Kirchhoff stress of the glassy phase ($\mathbf{S}_g$) following equation:

$$\mathbf{S}_g = J\mathbf{F}^{-1}\mathbf{T}_g^e\mathbf{F}^{-T}$$

(5)

The second Piola–Kirchhoff stress of an SMP was represented in terms of the volume fraction of the glassy phase ($\xi_g(T)$), as follows:

2 4

$$\mathbf{S} = (1 - \xi_g(T))\mathbf{S}_r + \xi_g(T)\mathbf{S}_g \tag{6}$$

where $\mathbf{S}_r$ and $\mathbf{S}_g$ are the second Piola–Kirchhoff stresses of the rubbery and glassy phases. The detailed equations for deriving the stresses in each phase are given in Table 1 and the material parameters used in the equations are presented in Table 2. The volume fraction is temperature-dependent and also affected by the temperature rate. The volume fraction of each phase was determined by measuring the storage modulus under different temperature-rate conditions. The detailed procedure used to determine the volume fraction is provided in *Section 2.2*.

Table 1 Basic equations of the constitutive model.

Governing equation		
Rubbery phase	Mooney–Rivlin hyperelastic spring	$\mathbf{S}_r = f_{\mathbf{S}_r}\left(\mathbf{C}_r^v, \mathbf{F}, \mathbf{I}\right)$ [32]
	Newtonian fluid	$k_r \overset{\&}{\mathbf{C}}_r = f_{\mathbf{C}_r^v}\left(\mathbf{C}_r^v, \mathbf{F}, \mathbf{I}\right), \ \ \phi_r = \frac{1}{2} k_r \overset{\&}{\mathbf{C}}_r : \overset{\&}{\mathbf{C}}_r$ [32]
Glassy phase	Linear elastic spring	$\mathbf{T}_g^e = \dfrac{1}{\det[\mathbf{F_e}]}[\Lambda tr(\mathbf{h})\mathbf{I} + 2G\mathbf{h}]$ [81]

	Langevin spring	$\mathbf{T}_g^b = \frac{1}{3} C_r \sqrt{N} \zeta^{-1} [\frac{\Lambda_{chain}^p}{\sqrt{N}}] \frac{(\Lambda_{p,g}^p)^2 - \frac{1}{3}\mathbf{I}_1}{\Lambda_{chain}^p}$ [81]
	Viscoplasticity	$\overset{g}{\mathbf{F}_g^{vp}} = \overset{g}{\gamma_p} N\mathbf{F}_p$ [81]
	Non-mechanical strain	$\dfrac{dE_{g,\,i}^{nm}}{dt} = \begin{cases} \alpha\xi_r\left(-E_{g,\,i}^{nm} + aE_i\right) & \text{for} \quad \left|aE_i\right| > \left|E_{g,\,i}^{nm}\right| \\ \alpha\xi_r\left(-E_{g,\,i}^{nm} + E_i\right) & \text{for} \quad \left|E_i\right| < \left|E_{g,\,i}^{nm}\right| \end{cases}$ [32]
Thermal strain	Noll's theorem	$\mathbf{F}_{thermal} = \gamma(\theta)\mathbf{I}$ for $\gamma(T) = \exp(\int_{T_0}^{T} \alpha(s)ds)$ [83]

Table 2 Material coefficients of the constitutive equation for a shape-memory polymer.

Rubbery phase	Spring constants of the first spring	$C_{10,r}^e$ = 3.791 [MPa]
		$C_{01,r}^e$ = -2.196 [MPa]
	Spring constants of the second spring	$C_{10,r}^v$ = 0.017 [MPa]
		$C_{01,r}^v$ = 0.019 [MPa]
	Bulk modulus	κ_r = 10.245 [GPa·s]

Glassy phase	Young's modulus	$E = 978.46$ [MPa]
	Poisson's ratio	$\nu = 0.33$
	Pre-exponential factor	$\dot{\gamma}_0 = 6.34 \times 10^3$ [1/s]
	Softening slope	$h = 710$ [MPa]
	Shear stress state ratio	$\dfrac{s_{ss}}{s_0} = 0.84$
	Zero stress level activation energy	$A = 229.19$ [K/MPa]
	Rubber modulus	$C_r = 8.86$ [MPa]
	Limiting chain stretch	$N = 2.78$
Shape memory strain	Formation rate of shape memory strain	$\alpha = 1$ [1/s]
	Ratio of shape memory strain to total deformation	$\beta = 0.985$

2.1.2 Effect of temperature rate on the volume fraction of each phase

For each temperature-rate condition, the normalized storage modulus measured in the cooling and heating directions formed a hysteresis loop (Figure 16). The storage modulus was measured under the frequency-controlled condition (1 Hz) in tensile mode. It was normalized once the driving force became constant; storage modulus values larger than the value used for the normalization were all set as 1. The area of the hysteresis loop widened with increasing temperature rate. Since polymer viscosity and chain mobility do not change immediately with variation of temperature, sufficient time is required for the polymer structure to evolve to the equilibrium state. Such a non-equilibrium dynamic effect is stronger in the vicinity of the T_g, which is reflected by the difference in storage modulus measured during cooling and heating [28]. Additionally, the difference increases with increasing temperature rate.
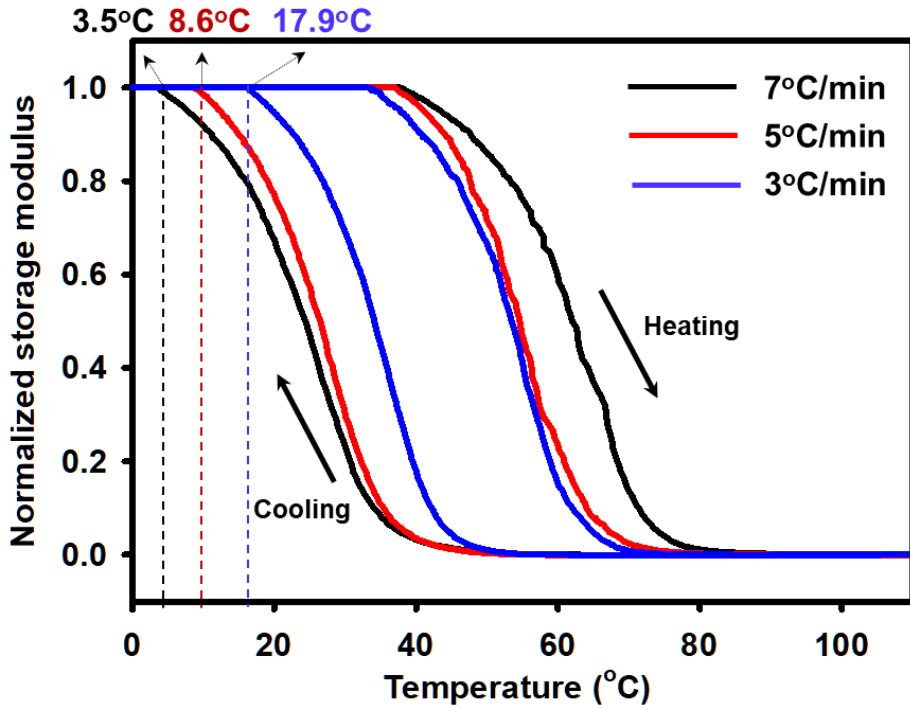
Figure 16 Normalized storage moduli of heating and cooling traces under different temperature-rate conditions.

The temperature-rate dependent volume fraction of each phase was characterized by normalized storage modulus curves. The normalized storage modulus (E'_{norm}) at $T = T_l$, where the glassy phase dominates, is given by following equation:

$$E'_{norm}(T_l) = \xi_g = 1 \tag{7}$$

Similarly, at $T = T_h$, where the rubbery phase dominates, the normalized storage modulus is given as follows:

$$E'_{norm}(T_h) = \xi_r - 1 = 0 \tag{8}$$

and at the intermediate temperature,

$$\xi_g = \frac{E'_{norm} - E'_{norm}(T_h)}{E'_{norm}(T_l) - E'_{norm}(T_h)} \tag{9}$$

The above equations exhibit how the volume fraction of the glassy phase, $\xi_g(T)$, can be obtained from experimental data. Note that E'_{norm} varies with temperature rate and differs under cooling and heating conditions.

2.1.3 Thermal deformation gradient

Assuming that the SMP is a thermally isotropic material, the thermal deformation gradient tensor is calculated according to Noll's theorem [83], as follows:

$$\mathbf{F}_{thermal} = \gamma(\theta)\mathbf{I}$$

(10)

$$\gamma(T) = \exp(\int_{T_0}^{T} \alpha(s)ds)$$

(11)

$$\varepsilon_{thermal}(T) = \int_{T_0}^{T} \alpha(s)ds$$

(12)

where $\mathbf{I}$ is the identity tensor and $\gamma(T)$ is a scalar-valued function of temperature, which is calculated by integrating the thermal expansion, $\alpha(s)$ (Equation (11)) [83, 84]. The thermal deformation gradient was calculated using experimentally measured thermal strains. The detailed procedure used to obtain the thermal strain is presented in *Section 3.2.* Figure 17 shows the measured thermal strain under various temperature rates. The variation in thermal strain with temperature change decreases with increasing temperature rate. Since the phase transition between the glassy and rubbery phases is retarded with increasing temperature rate [38], a slower cooling rate provides a lower transition temperature; alternatively, a higher heating rate gives a higher transition temperature (Figure 18). Due to the shift of the transition

3 1

temperature, the phase transition starts at a lower (higher) temperature under a faster cooling (heating) rate. As the temperature rate decreases, a relatively large phase transition occurs, which results in larger thermal strain at the intermediate temperature.
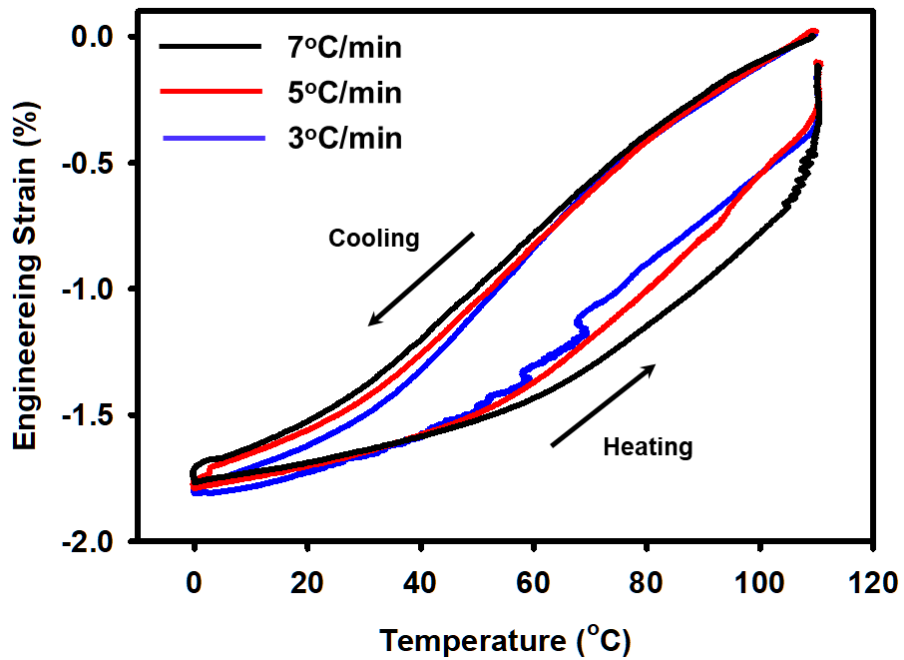
Figure 17 Thermal strain hysteresis loops under various temperature-rate conditions.
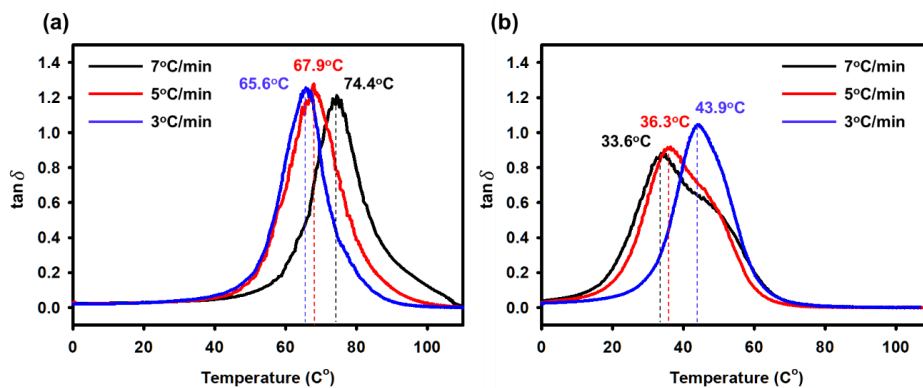
Figure 18 Tangent delta under different temperature-rate conditions. (a) Heating trace and (b) cooling trace.

2.2 Experimental

2.2.1 Material preparation

An SMP was synthesized by mixing an epoxy resin (EpoFix®; Struers, Denmark) with a curing agent (Jeffamine® D-230; Huntsman, USA). The weight ratio of resin to curing agent was 7:2. After the curing agent had completely mixed with the epoxy resin, the mixture was degassed in a vacuum oven for 1 h at room temperature and then poured into a mold and cured for 2 h at 110°C.

2.2.2. Dynamic mechanical behavior characterization

The thermomechanical behavior of the SMP was characterized using a dynamic mechanical analyzer (DMA Q800; TA Instruments, USA). The dimensions of the test

specimens were $30 \times 5 \times 0.8$ mm^3 (length × width × thickness). The gage length was set to 10 mm. The storage modulus and thermal strain were measured at ramping rates of 3°C/min, 5°C/min and 7°C/min. An SMP specimen was heated to 110°C, stabilized for 1 min, and then cooled to 0°C. The sample was then held for 10 min at 0°C and heated again to 110°C.

The storage modulus was measured at 1 Hz with an amplitude of 0.1%. It was normalized as described in *section 2.2*. The volume fraction of each phase was calculated using Equations (4–6). For the thermal strain, a static preload of 0.001 N was applied to the sample during the thermal cycles. One-way shape-memory behavior was characterized in the uniaxial tensile mode (Figure 19). A rectangular SMP specimen was stretched by 2.5% (ε_m) at 110°C. Then, the sample was cooled to 0°C while the strain was held constant. The strain was then released and the residual strain (ε_f) remained in the sample. The fixity was defined as $\varepsilon_f / \varepsilon_m$. The sample was reheated to 110°C, and the sample recovered by itself (ε_r); the recovery ratio was defined as $1 - \varepsilon_r / \varepsilon_m$.
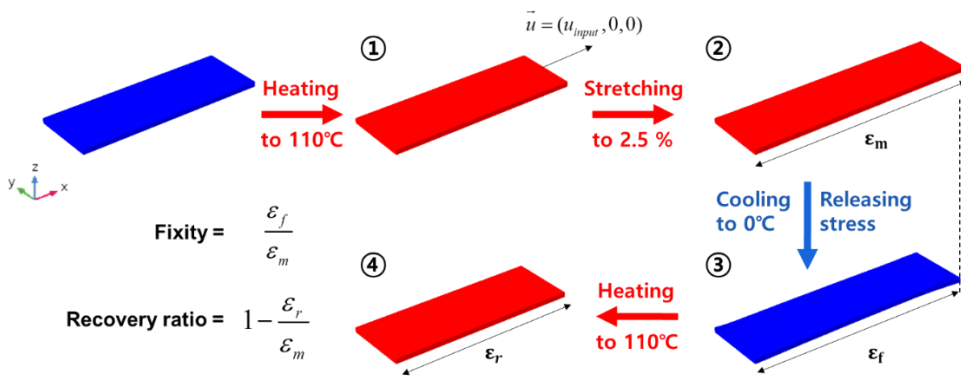
Figure 19 Shape-memory performance test for a rectangular shape-memory polymer (SMP) specimen.

2.2.3 Multi-dimensional testing of the SMP

A self-deployable antenna was designed to demonstrate the multi-dimensional deformation behavior of the SMP (Figure 20a-c) [85]. The deformation behavior was characterized using a universal testing machine (QUASAR 5; Galdabini, Italy) inside an environmental chamber. A flat circular antenna was fabricated for the deployment test. The diameter and thickness of the antenna were 150 and 1.1 mm, respectively. Shape changes of the antenna were recorded using a video camera and angle changes were measured from individual digital images for each step. The detailed deployment procedure was as follows (Figure 20d): (1) the antenna was heated to 110°C and then folded by 45° (θ_m); (2) the antenna was then cooled to 0°C, while

the deformation was fixed; (3) the temporary shape with a fold angle of θ_f was obtained after removing the folded device at 0°C; (4) the antenna was reheated to 110°Cand recovered its original shape (θ_r). The recovery ratio was defined as $1 - \theta_r / \theta_m$.
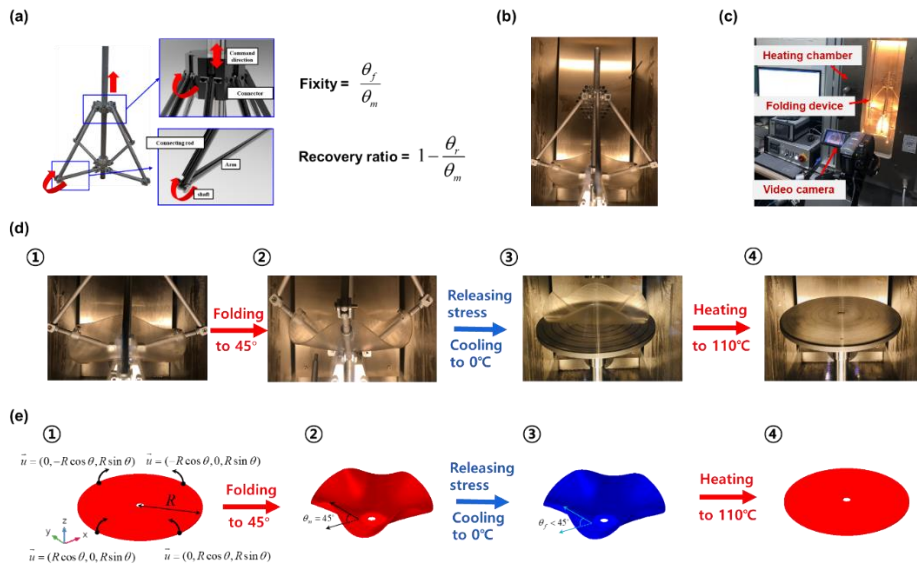
Figure 20 Deployment device and experimental set-up for the shape-memory polymer (SMP). (d, e) Procedure for folding and recovery. (a–c) Experimental set-up for the deployable antenna: (a) folding device; (b) SMP specimen mounted on the folding device inside an environmental chamber; (c) set-up for recording the deployment behavior.

2.3. Results and discussion

Uniaxial thermomechanical cycling tests and multi-dimensional deployment tests were simulated using the COMSOL^{TM} finite-element software package (COMSOL, Inc., Burlington, MA, USA). The governing equations listed in Table 1 were solved by the domain ordinary differential equation (ODE) solver. The material parameters for shape-memory strain were obtained from one-way shape-memory tests of rectangular specimens. Parameters α and β in Table 1 were calculated to minimize the difference between the experimental results and those predicted by the model; the least-squares error was 2.01%. Uni-axial tensile and creep tests were performed under isothermal conditions to obtain other material parameters. The determination of the material parameters is detailed in *Appendix A*. The simulated results were compared to the experimental data to validate the proposed temperature-rate dependent model.

2.3.1. Uniaxial thermomechanical shape-memory behavior

Uniaxial thermomechanical tests were simulated under different temperature-rate conditions (3°C/min, 5°C/min, and 7°C/min). The specimen was modeled using tetrahedral finite elements (2022 elements). The nodes on one side of the cross-section were all fixed (u = v = w = 0), while displacement of the nodes on the other side was proscribed by u = u$_{input}$ and v = w = 0 (Figure 20). Figure 21a shows the variation of strain according to the thermomechanical cycle steps. The sample was

3 7

pre-deformed by a strain of 2.5% (ε_m). and the strain was slightly reduced to about 2.2% (ε_f) after cooling and subsequently removing the constraint. The residual strain, ε_f, was independent of the temperature-rate condition. The thermal strain effect caused several features to appear during the recovery step. From 0°C to 36°C, when the glassy phase began to convert into the rubbery phase, the strain increased slightly to about 0.2%. With increasing temperature, the gradual increase in strain was dominated by thermal expansion of the glassy phase (Figure 21c–d). From 36°C to near the T_g, the mechanical strain rapidly decreased because of the release of the pre-deformation strain and larger thermal expansion coefficient of the rubbery phase. However, residual thermal strain (see Figure 21d) remained even after all of the glassy phase had transformed into the rubbery phase; therefore, the total strain was negative (Figure 21a). Beyond the T_g, residual thermal strain approached to zero. Therefore, the total strain almost fully recovered to 0% (Figure 21a).
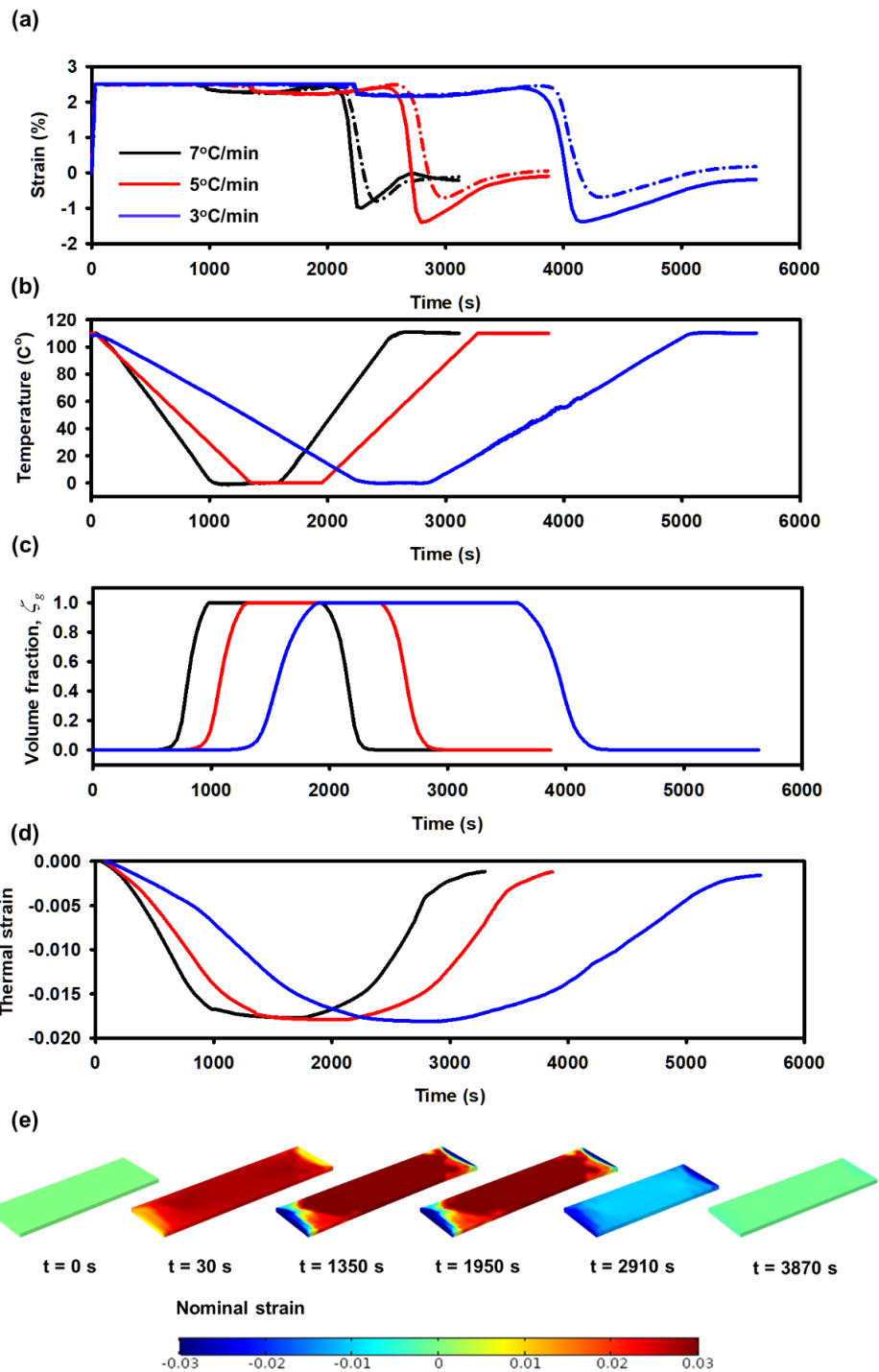
(a)

7°C/min
5°C/min
3°C/min

(b)

(c)

(d)

(e)

t = 0 s   t = 30 s   t = 1350 s   t = 1950 s   t = 2910 s   t = 3870 s

Nominal strain

-0.03   -0.02   -0.01   0   0.01   0.02   0.03

3 9

Figure 21 Experimental and simulation results of the uniaxial thermomechanical cycling test. (a) Engineering strain as a function of time (solid and dash–dot lines represent the simulation and experimental results, respectively), (b) input temperature, (c) volume fraction of the glassy phase as a function of time, (d) thermal strain from the thermal deformation gradient as a function of time, and (e) three-dimensional shape changes under the temperature-rate condition of 5°C/min. The color indicates the nominal strain.

Figure 22 shows the evolution of stress during a thermomechanical cycle. The specimen was more likely to contract during constrained cooling. Consequently, positive thermal stress was generated, which increased until the operating temperature reached 0°C. The amount of thermal stress depended on the temperature-rate condition; the slower the temperature rate, the higher the T_g, as discussed in *Section 2.3*. In other words, at a given temperature, the relative transformed volume fraction of the glassy phase increased with decreasing temperature rate. Thus, the thermal stress was more developed. This temperature-rate dependency was simulated (Figure 22). The results displayed in Figures 21 and 22 indicate that the current model simulated the temperature-rate dependent deformation behavior of the SMP with reasonable accuracy. In addition, higher temperature rate was also investigated, supporting the validity of the 3D constitutive model at higher temperature rate (see *Appendix A*).

Figure 22 Stress evolution during a uniaxial thermomechanical cycling test. (a) Engineering stress as a function of time (solid and dash–dot lines represent the simulation and experimental results, respectively) and (b) stress distribution in the geometry under the temperature rate condition of 5°C/min. Solid and dash–dot lines represent simulation and experimental results, respectively. The color indicates the nominal stress.

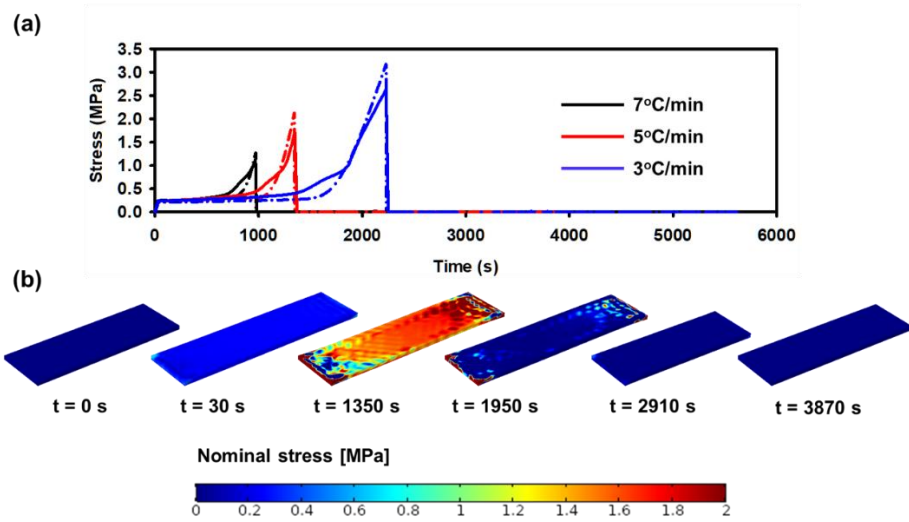### 2.3.2. Multi-dimensional deployment of SMPs

Multi-dimensional deployment tests were simulated under different temperature-rate conditions (3°C/min, 5°C/min, and 7°C/min) (Figure 23). The specimen was modeled using tetrahedral finite elements (4449 elements). The center of the antenna was fixed (u = v = w = 0). Four equally spaced points were identified in the edge and boundary conditions (Figure 20d). The same temperature profiles used in the uniaxial test were employed in these experiments. Shape changes of the antenna were captured using a video camera and angle changes were characterized from individual digital images for each step. In the deployment test, the strain variation was expressed as a change in angle. Unlike the uniaxial shape-memory behavior, the small increment of strain above the residual strain, ε_f, did not appear at the temperature where the glassy phase began to transform into the rubbery phase (Figure 23b). Additionally, the apparent compressive strain was negligible at temperatures above the T_g. Due to the existence of pre-compression, with a similar strain recovery path but in a different direction to pre-tension (to obtain the temporary shape), the dramatic changes in strain observed in the uniaxial tests were mitigated. Large pre-deformation strain (~35 %) reduced the thermal strain effect as shown in Figure 23d [27]. Summarizing, Figure 23 confirms that our model could simulate with reasonable accuracy the temperature rate-dependent multi-dimensional deformation behavior of an SMP.

(a)

(b)

(c)

(d)

Equivalent strain

Figure 23 Experimental and modeling results for the self-deployable antenna tests. (a) Input temperature, (b) change in antenna angle as a function of time under different temperature-rate conditions (solid and dash–dot lines represent the simulation and experimental results, respectively), (c–d) shape change under the temperature-rate condition of 5°C/min, (c) experimental images, and (d) simulation results. Solid and dash–dot lines represent the simulation and experimental results, respectively. The color indicates the equivalent strain, i.e.,

$$\varepsilon_{eq} = (2/3)\sqrt{(3/2)(e_{xx}^2 + e_{yy}^2 + e_{zz}^2) + (3/4)(\gamma_{xy}^2 + \gamma_{yz}^2 + \gamma_{zx}^2)}$$, where e is the deviatoric strain and γ is the shear strain.

2.4 Summary

A 3D constitutive model was developed to represent the temperature-rate dependent thermomechanical behavior of SMPs. Based on a two-phase (rubbery and glassy phases) phenomenological model, the variation of the temperature-dependent volume fraction of each phase was considered under different temperature-rate conditions. Moreover, the thermal strain was measured for various temperature rates and added to the model. The material parameters of the 3D constitutive equation were determined by measuring uniaxial tensile and creep behaviors. Finite-element simulations validated the developed constitutive models. Under different temperature-rate conditions, the thermomechanical deformation of a 1D rectangular slab and a 3D antenna were well-simulated by the model, from obtaining the temporary shape after pre-deformation above the transition temperature and

44

subsequent cooling below the transition temperature to recovering the original shape by reheating. Our developed constitutive model accurately captured the multi-dimensional temperature-rate dependent mechanical response of SMPs.

3. Constitutive modelling of anisotropic Liquid crystal elastomers

3.1. Needs for anisotropic modelling of LCEs

LCE is mainly composed of backbone polymer and mesogen. Backbone polymer shows isotropic mechanical properties like general polymers, but distinct properties based on the glass transition temperature (rubbery properties below T_g, and glassy properties above T_g). Mesogen, another component of LCE, binds to the backbone polymer and shows anisotropic behavior depending on its directionality. The direction of mesogen changes not only by external force, but also by temperature based on a specific temperature (T_i). Stretching to the LCE induce the transition from polydomain to monodomain alignment along the stretching axis, and the monodomain alignment is readily confirmed. The directionality of mesogen according to temperature changes differently from that of mesogen according to external force. When the directionality of mesogen exceeds T_i, it goes in a random direction regardless of the original directionality.

Herein, to modeling these distinct behaviors of LCEs, we developed three-phase constitutive model for LCEs. The backbone polymer, a component of LCE, was

modeled using the two-phase isotropic model. Based on the experimental results, the direction vector of mesogen was newly defined as a function of temperature and deformation. It is assumed that the mesogen behaves linearly elastically in the local coordinate, and tensor transformation is used to define the stress according to the temperature and deformation of the mesogen in the global coordinate. Lastly, for the two-way shape switching behavior of adaptable LCEs, a constant stress is critical to maintain the mesogen alignment in the LCEs network at low temperature (below Ti). However, In the case of monodomain LCE, mesogen alignment is maintained by UV curing without constant stress. To describe the driving force, the concept of the curing strain is adopted to the model. The curing strain is an element to explain shape memory effect.

3.2. Theory and experiments

3.2.1. Materials
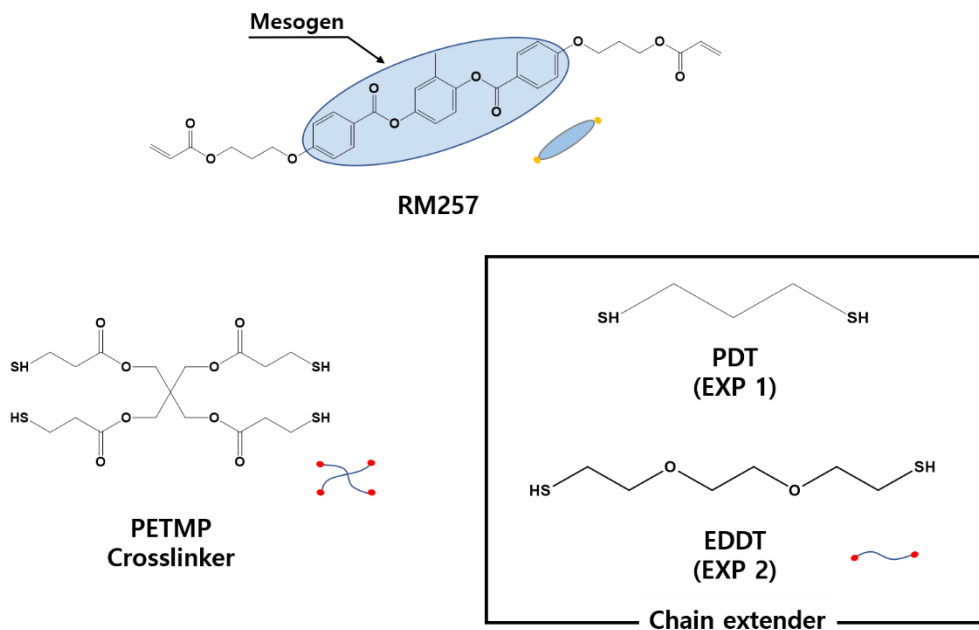
Figure 24 Chemical structure of monomers to produce main-chain LCE in this study. Mesogen monomer (RM257), Linear chain extender for linking mesogens with dithiol functional end group (PDT for exp1 and EDDT for exp2) and Crosslinking monomer with tetrathiol functional end group (PETMP) polymerized via Michael addition.

Main-chain liquid crystal elastomers were synthesized by a two-stage method. The first stage of the method is the thiol-acrylate Michael addition which led to the

formation of network among the monomers. The second stage is the radical photopolymerization to obtain the programmed shape of the LCE samples. During the first stage, diacrylate mesogen (RM 257, 64 wt%) and inhibitor 2,6-di-tert-butyl-4-methylphenol (BHT, 1.5 wt%) were dissolved in toluene (19.2 wt%) at 85°C for 30 mins. Subsequently thiol functional groups monomers, crosslinker (tetrathiol-PETMP,2.7 wt%), chain extender (1,3-PDT, 10.3 wt%), and photo-initiator (Phenylbis(2,4,6-trimethylbenzoyl) PPO, 1.5 wt%) were added to the mixture and reheated to 85°C for 3 mins. The ratio of the acrylate and thiol functional groups was calculated as 2 mol% in excess of acrylate functional groups than the stoichiometric amount. Shortly catalyst (Triethylamine, 0.77 wt%) was diluted. The solution was degassed under vacuum at 85°C for 2 mins for the fast thiol-acrylate Michael addition reaction. Then the solution was transferred to the glass mold where the two glass slides with 1 mm polytetrafluoroethylene spacers between slides. The mixture was polymerized at room temperature for 2 days, showing transparent elastomer film. Toluene was extracted under vacuum at 85°C until the material reached a stable weight. Elastomers were opaque white at room temperature indicating a liquid crystalline phase in the polydomain conformation.

In the second stage, monodomain LCEs (mesogen oriented to along direction) were formed by uniaxial stretching to the strain. After stretch to 100%, the radical photopolymerization was initiated by exposure to 365 nm wavelength ultraviolet light for up to 90 mins. during which excess acrylate groups reacted to form new

bonds in the network. In this way, monodomain mesogen alignment was achieved permanently by radical photopolymerization in the stretched shape, which provide the reversible shape memory properties of LCEs.

3.2.2. Dynamic properties of LCEs

To characterize the thermomechanical properties of the LCEs, dynamic mechanical analysis (DMA) was performed using a DMA tester (Model Q800, TA Instruments, New Castle, DE, USA). The glass transition temperature (Tg), storage modulus, and tan were obtained by tensile oscillation tests. A dynamic load (maximum load = 0.001 N, frequency = 1 Hz) was applied to each specimen. Samples were first heated to 150°C and stabilized for 10 min to reach thermal equilibrium. The storage modulus and tan delta were measured while changing the temperature from 150°C to -20°C, and the temperature equilibrium was maintained for each temperature (5°C increase for each step).
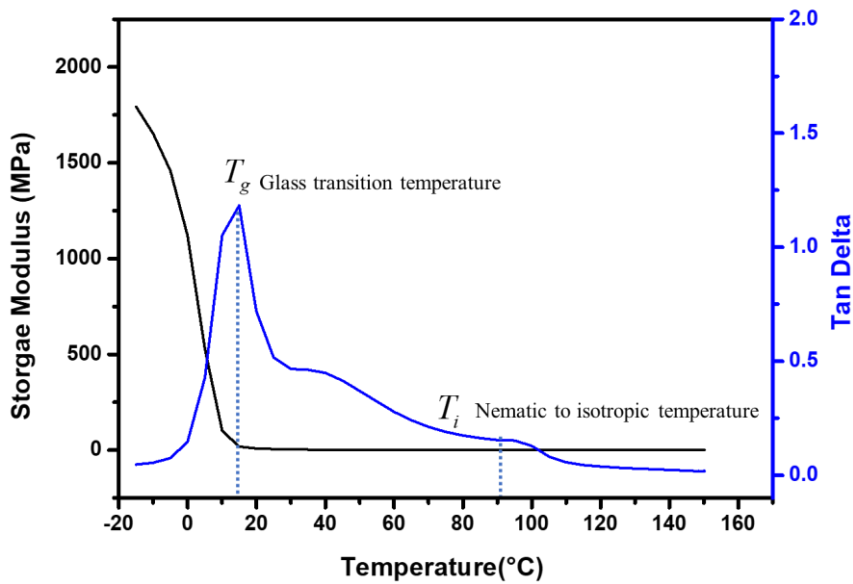
Figure 25 Dynamic mechanical analysis results of the LCE

Figure 25 shows the temperature dependence of the storage modulus and tan d. The glass transition temperature (Tg) was identified as the temperature corresponding to the peak of the tan delta curve, which was approximately 18°C. Likewise, epoxy based SMP, the soft elastic behavior of the rubbery phase is shown at a temperature higher than Tg, and the behavior of the brittle glassy phase is shown at a temperature below Tg. However, based on the temperature condition of Ti, LCE will show another phase transition. Ti (nematic to isotropic temperature) was identified at the distinct drop in the storage modulus at approximately 87.1C, often termed dynamic soft elasticity. At high

5 1

temperatures (above Ti), the axes of the anisotropic molecules are randomly distributed, and their centers of mass are randomly distributed. However, when the LCE is cooled to below Ti, the phase is converted to the nematic phase. The nematic phase is the simplest liquid crystal phase with least order. In this phase, the molecules tend to align along a particular direction.

3.2.3. Observation of anisotropic of mesogen
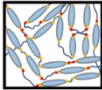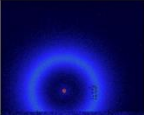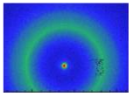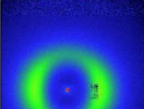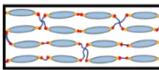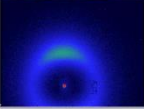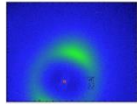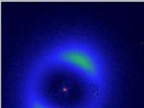
The wide-angle x-ray scattering (WAXS) measurements characterize the director field of the mesogen in LCEs under various temperature and strain conditions. The mechanism for the orientation of the mesogen, where the stress in along direction and various temperature are applied to LCEs, is presented by the 2D WAXS patterns in Figure 26-28.
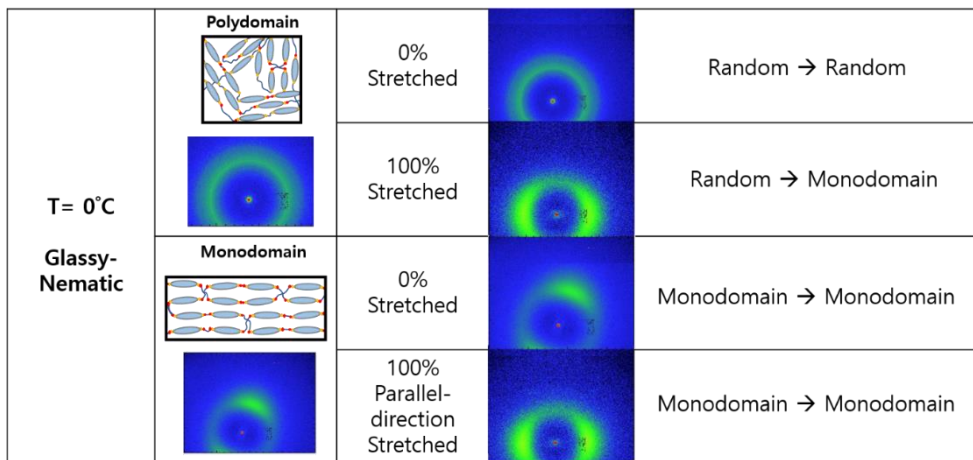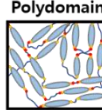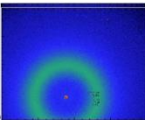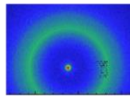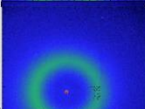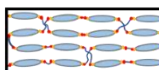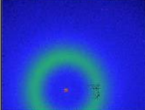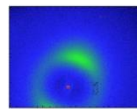
Figure 26 WAXS images of polydomain and monodomain LCEs at each phase

regions (glassy nematic) with strained and without strained.

Qualitatively, the isotropic pattern in the undeformed state reflects the randomly disordered polydomain alignment. In uniaxial stretching under Ti temperature region, the azimuthal redistribution of intensity of the pronounced scattering ring proceeds with stretching (an increase in x direction), indicating an increase in the mean orientational order parameter of the local nematic director in the larger strain (x) direction. In the glassy nematic phase, mechanical stretch leads to the temporary aligning; therefore, originally randomly ordered LCE is getting ordered in one direction (Figure 28). When the temperature is lowered to 0 ℃ from room temperature without stretching, direction of mesogens are still maintained as it was at room temperature.

	Polydomain	0% Stretched		Random → Random
T= 50℃		100% Stretched		Random → Monodomain
Rubbery-Nematic	**Monodomain**	0% Stretched		Monodomain → Monodomain
		100% Parallel-direction Stretched		Monodomain → Monodomain

Figure 27 Qualitative WAXS analysis of polydomain and monodomain LCE at 50°C (rubbery nematic phase) without stretching and with 100% stretch

	Polydomain	0% Stretched		Random → Random
T= 100℃		100% Stretched		Random → Random
Rubbery-Isotropic	**Monodomain**	0% Stretched		Monodomain → Random
		100% Parallel-direction Stretched		

Figure 28 Qualitative WAXS analysis of polydomain and monodomain LCE1 at 50°C (rubbery nematic phase) without stretching and with 100% stretch

Rubbery nematic phase shows the similar ordering trend as glassy nematic phase. In rubbery nematic phase, mechanical stretch brings about an alignment of mesogens while the temperature is not a prominent factor to change the mesogens direction. However, at temperatures above Ti, the direction distribution of mesogen changes. It was observed from figure 28 that the aligned mesogens are getting randomly oriented when the temperature is above T_i. In other words, in isotropic and rubbery phase, regardless of the mechanical stretch, originally randomly ordered LCEs are still in random phase. This implies that the temperature is a more dominant factor than the mechanical stretch to determine the mesogen ordering in this phase. In Figure 28, case 3, it can be qualitatively confirmed that the orientation of mesogen is randomly distributed even if 100% stretch is given. Quantitatively, degree of Orientation can be expressed by a numerical representation which means how much liquid crystal molecules are aligned in the same direction. Full Width Half Maximum (FWHM) was used to determine the degree of orientation by quantifying the azimuthal spread obtained through WAXS. The degree of orientation (F) is defined as;
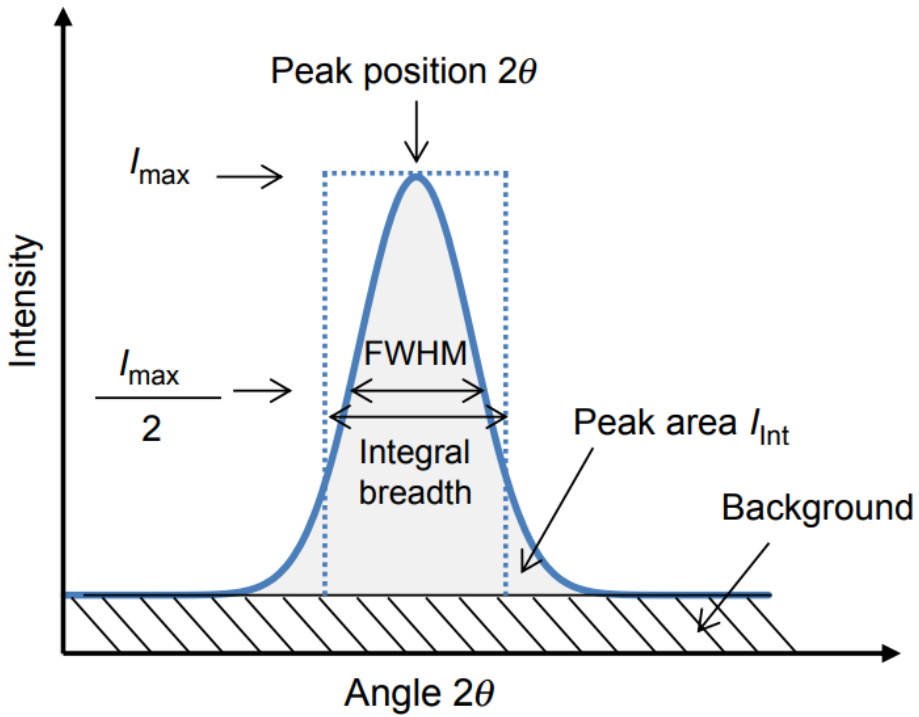
Figure 29 Diffraction peak and information content from the XRD experiment.
The imagine is obtained from the reference [53]

$$F = (180 - Wh) / 180 \times 100 \, (\%) \qquad \textbf{(13)}$$

Figure 30 shows the experimental results of the orientation of the mesogen at various

temperature conditions. Each polydomain LCE samples is stretched to 100%. Under

Ti temperature region, the value of the degree of the orientation is maintained as

around 60% due to mechanical stretch. However, When the temperature is raised to Ti, the mobility of the mesogen becomes active. Therefore, the regularity of the mesogenic arrangement disappears. After that, when temperature rises above Ti, the orientation of mesogen is randomly distributed even if 100% stretch is given. In addition to that, as the temperature approaches Ti, the change of degree of orientation influenced by thermal energy is greater than the mechanical strain. In other words, as the temperature is closer to Ti, temperature becomes a more dominant factor to determine the degree of orientation of mesogens. In this way, we assumed that there will be an inflection point of temperature at which the effect of temperature is more dominant in the direction of mesogen than that of mechanical force.
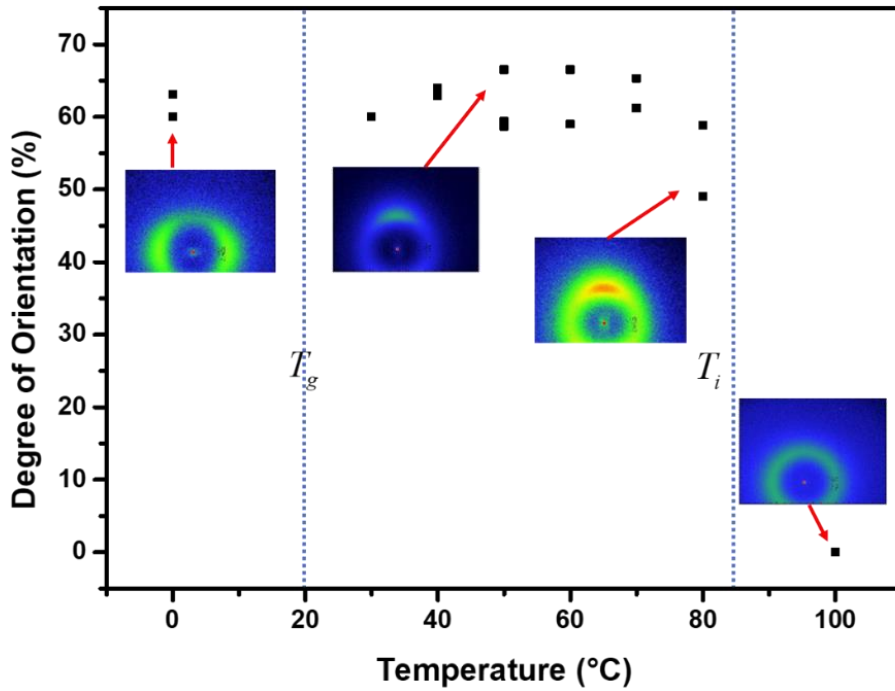
Figure 30 Degree of Orientation of stretched Polydomain LCEs

3.2.4. Constitutive model of LCEs

LCE is mainly composed of backbone polymer and mesogen. Backbone polymer shows isotropic mechanical properties like general polymers, but distinct properties based on the glass transition temperature (rubbery properties below T_g, and glassy properties above T_g).

Therefore, based on the two-phase isotropic rate-dependent model, a new

approach constitutive model for LCE was developed considering anisotropic properties of mesogen. Based on the experimental results, the direction vector of mesogen was newly defined as a function of temperature and deformation. It is assumed that the mesogen behaves linearly elastically in the local coordinate, and tensor transformation is used to define the stress according to the temperature and deformation of the mesogen in the global coordinate. Lastly, to describe the two-way behavior of monodomain LCEs, the constitutive model introduces the curing strain concept. Stored strain acts as a drive force for the formation of a monodomain of mesogen. The anisotropic constitutive model is validated by simulating the thermo-mechanical behavior of LCE under various boundary conditions.
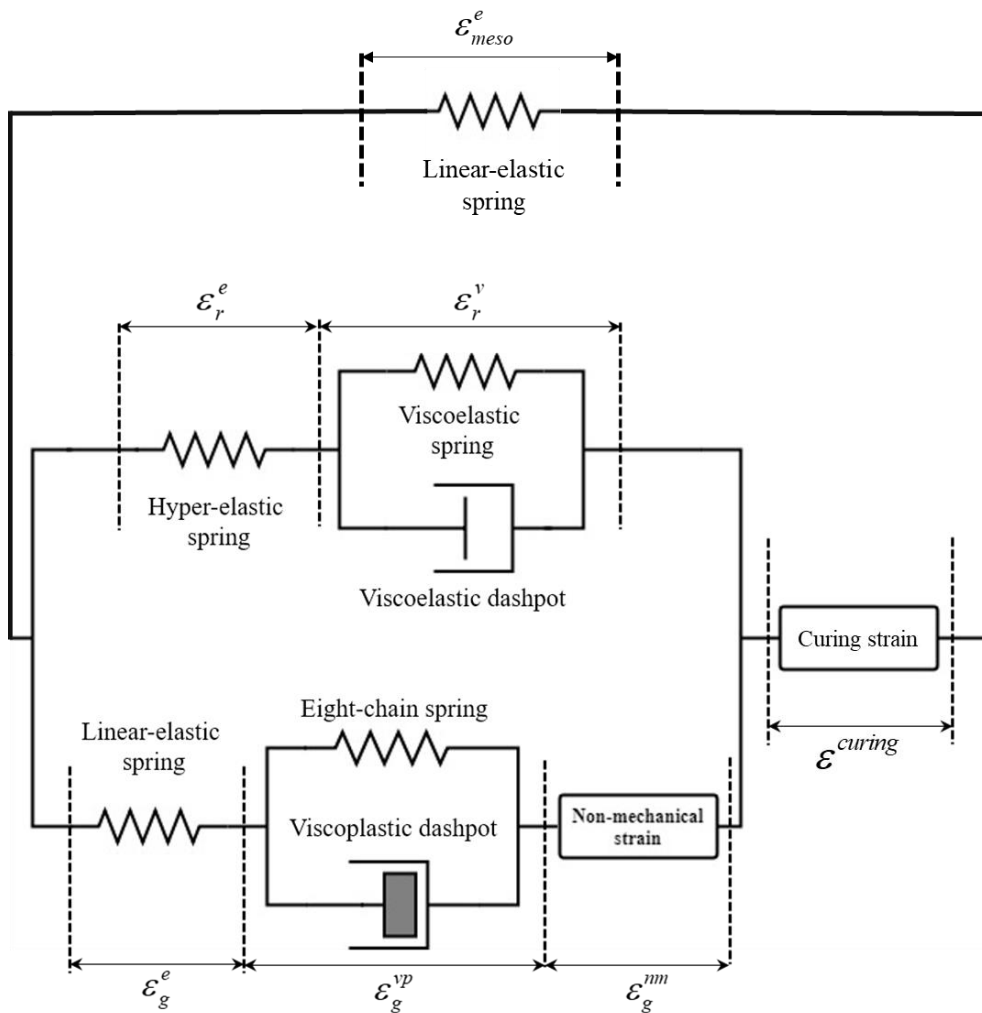
Figure 31 Constitutive model of LCEs

Table 3 Material coefficients of the constitutive equation for a liquid crystal elastomers

Rubbery phase	Spring constants of the first spring	$C^e_{10,r} = 0.001$ [MPa]
		$C^e_{01,r} = 0.0116$ [MPa]
	Spring constants of the second spring	$C^v_{10,r} = 0.0497$ [MPa]
		$C^v_{01,r} = 0.0011$ [MPa]
	Bulk modulus	$\kappa_r = 0.6296$ [MPa·s]
Glassy phase	Young's modulus	$E = 57.5$ [MPa]
	Poisson's ratio	$\nu = 0.33$
	Pre-exponential factor	$\dot{\gamma}_0 = 2.1 \times 10^{15}$ [1/s]
	Softening slope	$h = 500$ [MPa]
	Shear stress state ratio	$\dfrac{s_{ss}}{s_0} = 0.78$
	Zero stress level activation energy	$A = 2.4 \times 10^{-4}$ [K/MPa]
	Rubber modulus	$C_r = 18$ [MPa]

	Limiting chain stretch	$N = 2.78$
Shape memory strain	Formation rate of shape memory strain	$\alpha = 1$ [1/s]
	Ratio of shape memory strain to total deformation	$\beta = 0.985$
Material parameters of mesogen	Young's modulus	$E = 0.03$ [MPa]
	Poisson's ratio	$\nu = 0.33$
Curing strain	Formation rate of curing strain	$\gamma = 1$ [1/s]
	Ratio of curing strain to total deformation	$\beta = 0.985$

3.2.4.1. Constitutive model of LCE matrix

The shape memory behavior of an LCEs under nematic-to-isotropic transition temperature (Ti) is mainly dependent on the properties of the backbone polymer; shape recovery and fixation are controlled by the transition between rubbery and glassy phases of the backbone polymer. The volume fraction of these phases depends on temperature (Tg), and thus thermomechanical modeling should be conducted first to simulate the phase transition of the LCEs. In this work, we adopted a 3D constitutive equation for an LCEs. The second Piola–Kirchhoff stress of an LCEs

was represented in terms of the volume fraction of the glassy phase ($\xi_g(T)$), as

follows:

$$\mathbf{S}_{bakcbone} = (1 - \xi_g(T))\mathbf{S}_r + \xi_g(T)\mathbf{S}_g \tag{14}$$

where $\mathbf{S}_r$ and $\mathbf{S}_g$ are the second Piola–Kirchhoff stresses of the rubbery and

glassy phases.

3.2.4.2. Constitutive model of mesogen
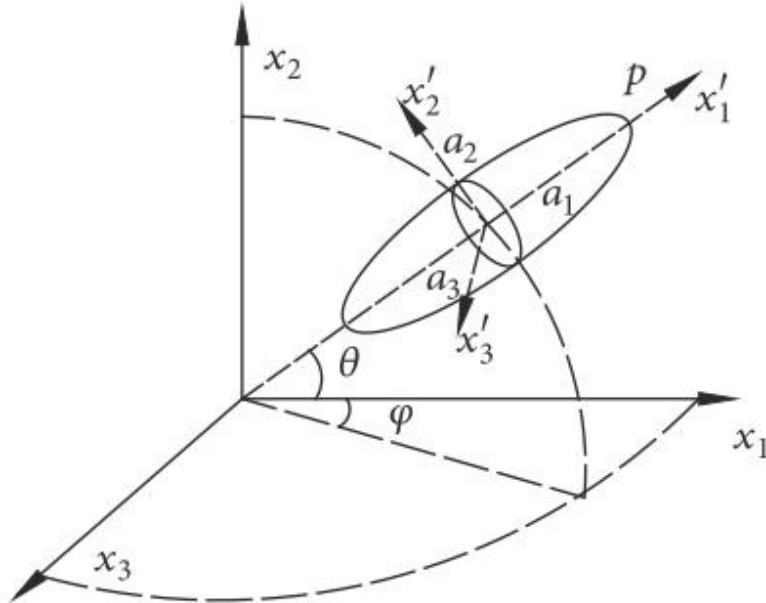
Figure 32 Direction vector **n** of a spatially oriented mesogen (Gain from

reference [86])

The direction vector of mesogen n can be described as $\mathbf{n} = (\cos\theta, \sin\theta\cos\varphi, \sin\theta\sin\varphi)$, where θ and φ are the Euler angles as shown in Figure 32. x_1, x_2, and x_3 are the three directions of the global coordinates, while x_1', x_2' and x_3' are the three directions of the local coordinates. Below T_i, backbone polymers are densely cross-linked, the director **n** cannot rotate freely, but changes through convection due to elastic strain. The director vector ($\mathbf{n}_{deformed}$) is updated using the deformation

gradient from the increment deformation as:

$$\mathbf{n}_{deformed} = \frac{\mathbf{F} \cdot \mathbf{n}_{ref}}{\left| \mathbf{F} \cdot \mathbf{n}_{ref} \right|}$$

(15)

Above T_i, backbone polymers are weakly cross-linked, the director vector of mesogen existed randomly, and the material exhibits isotropic mechanical effects. Therefore, θ and φ were defined by giving a random seed to each integration point, and the direction vector at a temperature above T_i was defined as follows.

$$\mathbf{n} = (\cos \theta_{Ti}, \sin \theta_{Ti} \cos \varphi_{Ti}, \sin \theta_{Ti} \sin \varphi_{Ti})$$

(16)

Where, θ_{Ti} and φ_{Ti} are random angle to each integration points. Through WAXS experimental results, it was confirmed that the orientation of the mesogen follows the deformation at the temperature before Ti,and is randomly distributed regardless of the deformation after Ti.

$$\cos^{-1}(\mathbf{n}_{1,deformed}) = \theta_{deformed}$$

(17)

$$\cos^{-1}\left(\frac{\mathbf{n}_{2,deformed}}{\sin \theta_{deformed}}\right) = \varphi_{deformed}$$

(18)

$$\xi_{ti}\theta_{Ti} + (1-\xi_{ti})\theta_{deformed} = \theta_{new} \tag{19}$$

$$\xi_{ti}\varphi_{Ti} + (1-\xi_{ti})\varphi_{deformed} = \varphi_{new} \tag{20}$$

$$\mathbf{n}_{new} = (\cos\theta_{new},\ \sin\theta_{new}\cos\varphi_{new},\ \sin\theta_{new}\sin\varphi_{new}) \tag{21}$$

In this case, the general framework in the previous section remains valid. $\mathbf{u}_i$ and $\mathbf{u}_j'$ are the unit vectors of the global coordinates (x_1, x_2, and x_3) and local coordinates (x_1', x_2' and x_3'), respectively. A relationship between them can be constructed as follows

$$\mathbf{u}_i = \boldsymbol{\alpha}_{ji}\mathbf{u}_j' \tag{22}$$

$$\boldsymbol{\alpha}_{ji} = \begin{bmatrix} \cos\varphi & \sin\theta\cos\varphi & \sin\theta\sin\varphi \\ -\sin\theta & \cos\theta\cos\varphi & \cos\theta\sin\varphi \\ 0 & -\sin\varphi & \cos\varphi \end{bmatrix} \tag{23}$$

Where, α_{ji} is the transformation matrix, and the local elastic matrix is as follows:

$$\mathbf{E}_{local} = \begin{bmatrix} \mathbf{E}_{1111} & \mathbf{E}_{1122} & \mathbf{E}_{1133} & \mathbf{E}_{1112} & \mathbf{E}_{1123} & \mathbf{E}_{1113} \\ \mathbf{E}_{1122} & \mathbf{E}_{2222} & \mathbf{E}_{2233} & \mathbf{E}_{2212} & \mathbf{E}_{2223} & \mathbf{E}_{2213} \\ \mathbf{E}_{1133} & \mathbf{E}_{2233} & \mathbf{E}_{3333} & \mathbf{E}_{3312} & \mathbf{E}_{3323} & \mathbf{E}_{3313} \\ \mathbf{E}_{1112} & \mathbf{E}_{2212} & \mathbf{E}_{3312} & \mathbf{E}_{1212} & \mathbf{E}_{1223} & \mathbf{E}_{1213} \\ \mathbf{E}_{1123} & \mathbf{E}_{2223} & \mathbf{E}_{3323} & \mathbf{E}_{1223} & \mathbf{E}_{2323} & \mathbf{E}_{2313} \\ \mathbf{E}_{1113} & \mathbf{E}_{2213} & \mathbf{E}_{3313} & \mathbf{E}_{1213} & \mathbf{E}_{2313} & \mathbf{E}_{1313} \end{bmatrix} \qquad (24)$$

$$\mathbf{E}_{local} = \frac{E}{(1+\upsilon)(1-2\upsilon)} \begin{bmatrix} 1-\upsilon & \upsilon & \upsilon & 0 & 0 & 0 \\ \upsilon & 1-\upsilon & \upsilon & 0 & 0 & 0 \\ \upsilon & \upsilon & 1-\upsilon & 0 & 0 & 0 \\ 0 & 0 & 0 & \dfrac{1-2\upsilon}{2} & 0 & 0 \\ 0 & 0 & 0 & 0 & \dfrac{1-2\upsilon}{2} & 0 \\ 0 & 0 & 0 & 0 & 0 & \dfrac{1-2\upsilon}{2} \end{bmatrix} \qquad (25)$$

A relationship between the elastic tensor $\mathbf{E}_{global}$ of the global coordinates and $\mathbf{E}_{local}$ of the local coordinates can be described as follows:

$$E_{ijkl}^{global} = \alpha_{i'i}\alpha_{j'j}\alpha_{k'k}\alpha_{l'l}E_{i'j'k'l'}^{local} \qquad (26)$$

where $\alpha_{i'i}, \alpha_{j'j}, \alpha_{k'k}, and \ \alpha_{l'l}$ are the elements of the transformation matrix $\boldsymbol{\alpha}_{ji}$. E_{ijkl}^{global} and E_{ijkl}^{local} are the elements of the corresponding elastic tensor. Using the linear elastic theory, the second Piola-Kirchhoff stresses of mesogen is obtained by the following equation:

$$\mathbf{s}_{global,mesogen} = \begin{bmatrix} \mathbf{E}_{1111}^{global} & \mathbf{E}_{1122}^{global} & \mathbf{E}_{1133}^{global} & \mathbf{E}_{1112}^{global} & \mathbf{E}_{1123}^{global} & \mathbf{E}_{1113}^{global} \\ \mathbf{E}_{1122}^{global} & \mathbf{E}_{2222}^{global} & \mathbf{E}_{2233}^{global} & \mathbf{E}_{2212}^{global} & \mathbf{E}_{2223}^{global} & \mathbf{E}_{2213}^{global} \\ \mathbf{E}_{1133}^{global} & \mathbf{E}_{2233}^{global} & \mathbf{E}_{3333}^{global} & \mathbf{E}_{3312}^{global} & \mathbf{E}_{3323}^{global} & \mathbf{E}_{3313}^{global} \\ \mathbf{E}_{1112}^{global} & \mathbf{E}_{2212}^{global} & \mathbf{E}_{3312}^{global} & \mathbf{E}_{1212}^{global} & \mathbf{E}_{1223}^{global} & \mathbf{E}_{1213}^{global} \\ \mathbf{E}_{1123}^{global} & \mathbf{E}_{2223}^{global} & \mathbf{E}_{3323}^{global} & \mathbf{E}_{1223}^{global} & \mathbf{E}_{2323}^{global} & \mathbf{E}_{2313}^{global} \\ \mathbf{E}_{1113}^{global} & \mathbf{E}_{2213}^{global} & \mathbf{E}_{3313}^{global} & \mathbf{E}_{1213}^{global} & \mathbf{E}_{2313}^{global} & \mathbf{E}_{1313}^{global} \end{bmatrix} \begin{bmatrix} \varepsilon_x \\ \varepsilon_y \\ \varepsilon_z \\ 2\varepsilon_{xy} \\ 2\varepsilon_{yz} \\ 2\varepsilon_{xz} \end{bmatrix} \qquad (27)$$

3.2.4.3. Derivation of curing strain component

For The two-way shape switching behavior of a polydomain adaptable LCEs, a constant stress is critical to maintain the mesogen alignment in the LCEs network at low temperature (below T_i). However, In the case of monodomain LCE, mesogen alignment is maintained by UV curing without constant stress. To describe the driving force, the concept of the curing strain is adopted to the model. The curing

strain is an element to explain shape memory effect. During stretching under UV curing condition, the stored strain is generated (Equation ~). But its role does not appear because the role of stored strain is only to store the strain caused by UV curing.
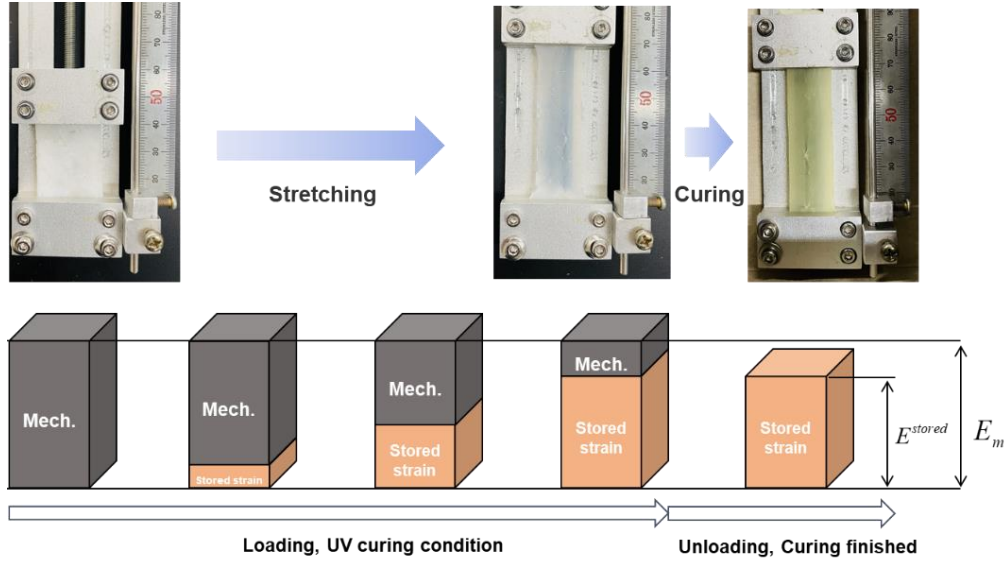
Figure 33 Schematic description of the stored strain.

$$\frac{dE^{stored}}{dt} = \alpha\left(-E^{stored} + aE_m\right) \text{ for UV condition} \qquad \textbf{(28)}$$

where, α is formation rate of stored strain (α is 0, when LCE is not exposed to UV), and a is the amount of the stored strain. The stored strain is converted to curing strain and the stored strain value does not change unless UV curing occurs. Through this process, the programming step by UV curing was described. The curing strain is calculated as follows:

$$\frac{dE^{curing}}{dt} = \begin{cases} \gamma\xi_{ti}\left(-E^{curing} + E_m\right) & \text{for} \quad |E_m| < |E^{curing}| \\ \gamma\xi_{ti}\left(-E^{curing} + \beta\xi_{ti}E^{stored}\right) & \text{for} \quad |E_m| > |E^{curing}| \text{ and } |E_{stored}| > |E^{curing}| \end{cases} \quad \textbf{(29)}$$

Where, γ is Formation rate of the curing strain, and β is amount of the stored strain. When LCE is heated, LCE goes back to its original shape, and it is in stress-free state now because the curing strain gradually disappears, the LCE sample contracts due to entropy elasticity. As temperature decreases below tr Ti, the polymer chains in LCE lose their mobility, but the orientation of the mesogen aligned to programmed direction. The curing strain does role of these programmed strain; Stored strain acts as a drive force for the formation of a monodomain of mesogen at low temperatures.

Heating condition (temperature rise to T_i)

If E_m decreases under E_{curing},

then, E_{curing} decreases.
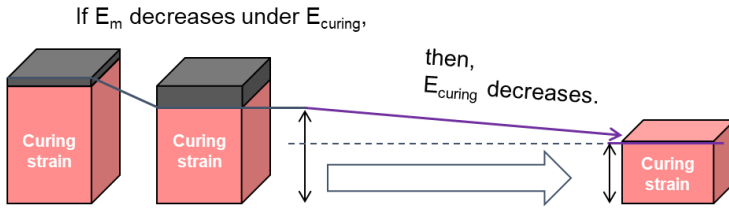
Cooling condition (temperature fall under T_i)

E_{curing} increased to E_{stored}.
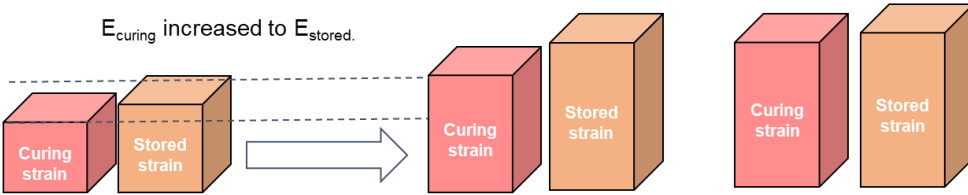
Figure 34 Schematic description of the curing strain. (a) Generation and extinction of non-mechanical strain for each step and its role related to the shape of LCEs.

From these profile of the curing strain, two important rules can be caught. the rate of the curing strain depends on temperature, and the stored strain does not change. During UV curing step, the curing strain is formed up to certain ratio (which will be written as β) of total deformation (same as the stored strain). And in heating step, total deformation decreases, and the curing strain also decreases. This indicates that the curing strain depends on total deformation. Last, the curing strain also increases to the certain strain (stored strain), also the total deformation gradient increased due to the curing strain.

3.3. Simulation and experimental results of LCEs

3.3.1. Simulation and experimental results of the Mesogen orientation
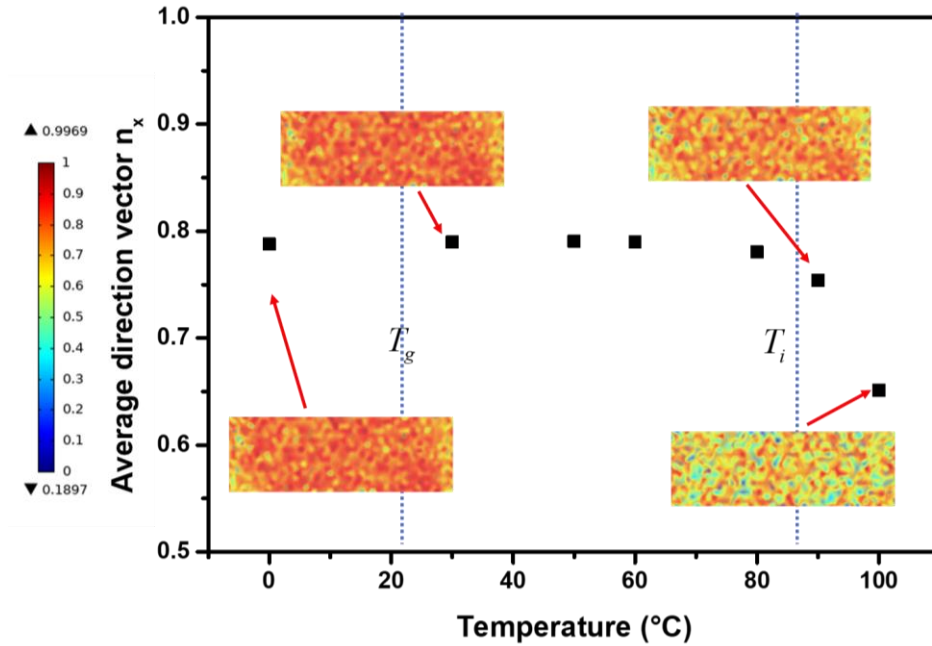
Figure 35 Simulation results of the mesogen orientation

Figure 35 shows simulation results of LCEs for each temperature under 100% stretch. Each simulation result expressed the average value of the direction vector in the x direction at all integration points. The director rotation gradually proceeds with stretching, and it reached 60% degree of orientation (Average direction vector = 0.8) at 100% stretch. It is evident that the stretching is accompanied by director rotation

for LCE under Ti temperature region, and the director rotation proceeds in an inhomogeneous manner.

However, it was observed from figure 35 that the aligned mesogens are getting randomly oriented when the temperature is above Ti. In other words, in isotropic and rubbery phase, regardless of the mechanical stretch, originally randomly ordered LCEs are still in random phase. This implies that the temperature is a more dominant factor than the mechanical stretch to determine the mesogen ordering in this phase.

3.3.2. Mechanical behavior of LCEs

Tensile loading of LCEs results in the unique deformation in which the polydomain structure evolves towards a monodomain by mesogen or domain reorientation to the tensile axis. Therefore, stress relaxation experiment and simulation were conducted to identify the inflection temperature point where the change of degree of orientation of mesogens in LCEs gets more influenced by thermal energy than the mechanical strain. Concretely explaining, Therefore, we came up with the idea of interpreting the alignment of mesogens in a mechanical way. The relaxation of the liquid crystal material consists of two stages: stress relaxation and orientation relaxation [4]. The first step is stress relaxation is the relaxation of polymer chains which occurs equally in both isotropic or anisotropic phases. The second step, orientation relaxation, is a relaxation that restores the mesogen to a thermodynamically stable equilibrium, which is only observed in anisotropic phase. It is believed that the presence of

relaxation implies the presence of orientation relaxation. If the relaxation is not observed from the certain temperature, that means the intrinsic energy of mesogen provided by the thermal energy is big enough to prevent the relaxation. Therefore, it is able to find the inflection temperature point at which the temperature affects more dominantly than the given mechanical strain by scanning the presence of relaxation. Shortly, relaxation rate (time) of the nematic director fluctuations increases (decreases) with strain along the director. Relaxation times trended toward shorter with increasing temperature due to increased network and mesogen mobility.
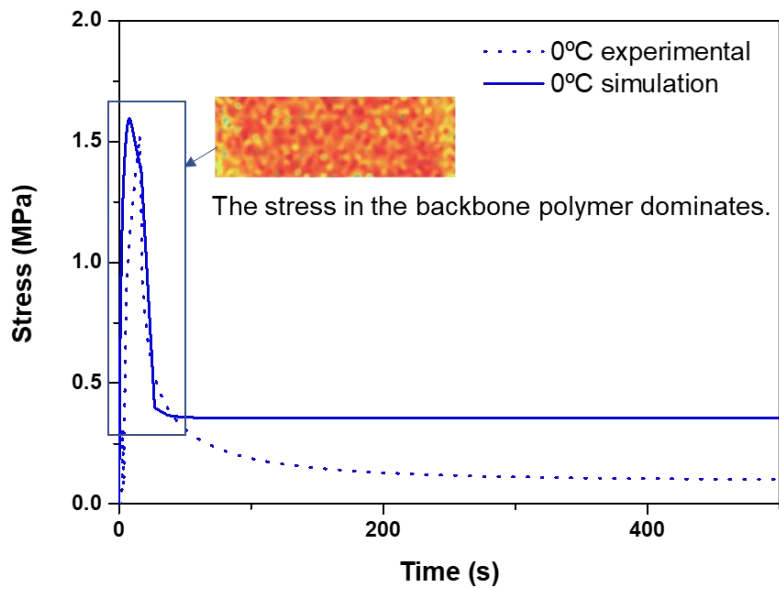
Figure 36 Stress relaxation test and simulation results (Low temperature below Tg)
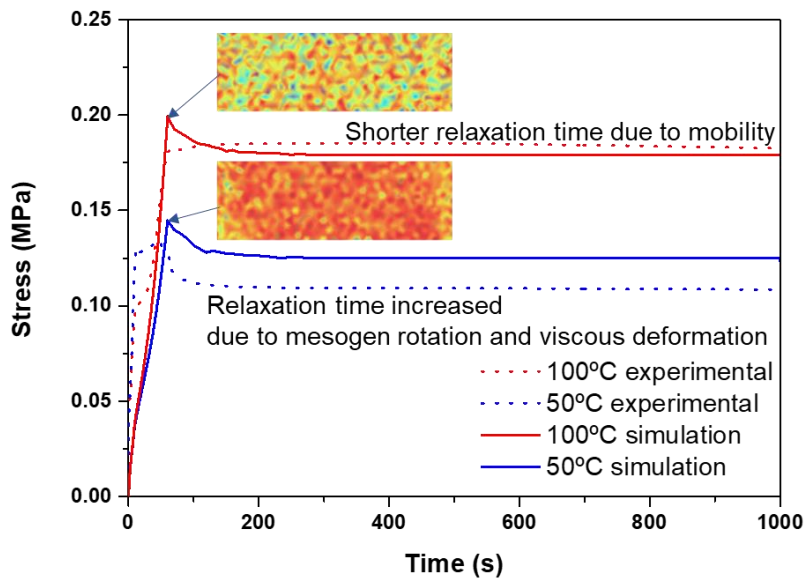
Figure 37 Stress relaxation test and simulation results (High temperature upon Tg)

Stress relaxation test was performed at various temperatures under isothermal condition. Figure 37 shows that the stress relaxation test at various temperature (above T_g). In the glassy regime below Tg, network deformation was restricted to deformation mechanisms of the backbone polymer. In the rubbery nematic range between T_g and T_i, mesogen rotation and viscous deformation of the backbone polymer dissipated energy. However, as temperature increased above T_i, there is a sharp drop infers the relaxation of polymer chains that links mesogen monomers, followed by the increase of stress implies the mesogen rotation is hindered by thermal energy. Hence, the inflection point where the degree of orientation becomes

more influenced by thermal energy than the mechanical strain was determined.

3.3.3. Two-way shape memory simulation of polydomain LCEs

In this section, the two-way shape memory behavior of polydomain LCEs under constrained stress was simulated using the constitutive model in figure 38.   All the nodes on the left cross-section (perpendicular to the loading axis (x-axis)) were fixed (u = v = w = 0), while the constant load was prescribed on the opposite side with the boundary conditions (v = w = 0). With boundary conditions given, the temperature was periodically changed. An initial temperature(120°C) was given to LCEs, then, it was cooled down to -20°C (cooling rates -3°C/mins) and maintained for about 10 mins. followed by heating up to 120°C and duration about 10mins. Total second period of temperature was input as shown in figure 38.

LCE properties were measured with constant stress actuation tests on the DMA machine. Prior to testing, the LCE sample (20 mm x 6 mm x 1 mm) was heated to 120°C and held for 10 mins to equilibrate the material temperature. After this ramp, an engineering stress of 0.35 MPa was applied and held constant for the remainder of the test. To achieve actuation, the same temperature conditions were applied to LCEs. The strain of the sample was monitored simultaneously with the temperature.

Figure 38 presents the simulated results of the two-way shape memory behavior of LCEs under constrained stress, showing the strain periodicity due to the driving force

(constant load input). For about 60 seconds (at initial temperature 120°C), the LCEs showed the creep behavior because mechanical behaviors of LCEs at high temperature were dependent on the load magnitude applied, i.e., the creep strain increased as the load increased. As the temperature was changed periodically, the periodic and repeatable strains were predicted as shown in figure 39, i.e., increased strain upon cooling and decreased strain upon heating. The applied bias stress drives the formation of a monodomain of liquid crystals when cooling the network below Ti, which leads to the elongation of the material in the same direction. Upon heating above Ti, the favorable intermolecular forces acting among mesogens are disrupted and the LCE sample contracts due to entropy elasticity. It can be claimed that the current constitutive model can predict such constrained stress recovery phenomena properly, the mechanism of which can be explained by the orientation of mesogens as follows.
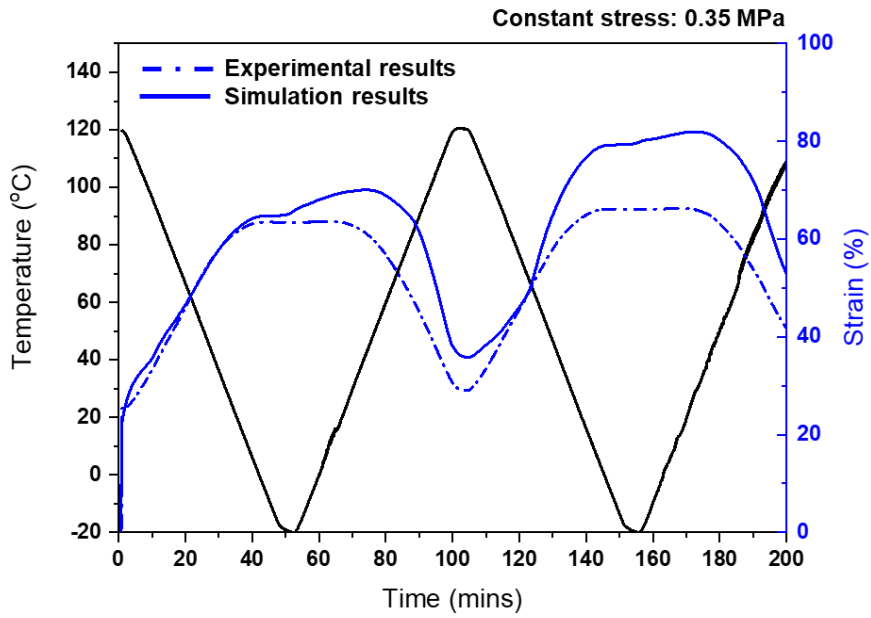
Figure 38 Simulation and experimental result of two-way shape memory behaviors
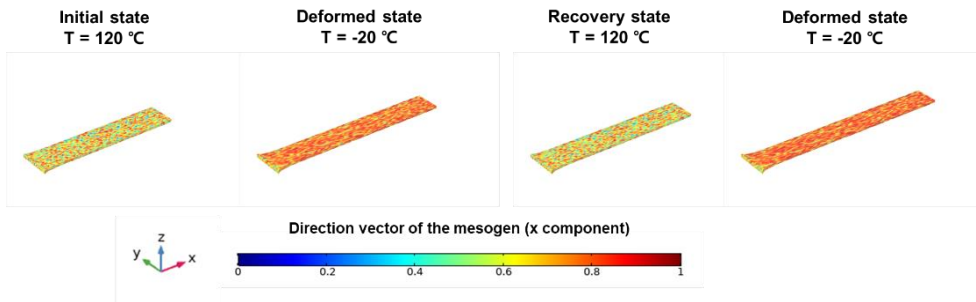
Figure 39 Simulation result of two-way shape memory behaviors

(Color represent the direction of the mesogens)

7 8

The total strain was plotted with the orientation of the mesogen during the repeated cyclic temperature under the constant load in Figure 38. The repeatable strain according to the cyclic temperature can be explained by the orientation of the mesogen. Under the constant load at $T = T_h$, the LCEs showed the creep behavior because LCEs has viscoelastic behavior. As the LCE is cooled down, the volume fraction of glassy phase increases and the mesogen oriented to deformation direction. When cooling the network below Ti, the stress at this state is smaller than the constant input load (stress) because the stress developed in the rubbery phase disappears as the volume fraction of the rubbery phase decreases, causing unbalance the force equilibrium. To regain the force equilibrium (under constant load applied), the strain of the SMP increases. Also, the formation of a monodomain of mesogen leads to the elongation of the material in the same direction. Upon heating, the mechanical strain decreases as the rubber phase increases, overall bringing about decreased strain of LCEs.

3.3.4. Two-way shape memory simulation of monodomain

LCEs

Two-way shape memory behavior of the monodomain were measured using DMA machine without any external force conditions. the LCE sample (20 mm x 6 mm x 1 mm) was heated to 120°C and held for 10 mins to equilibrate the material temperature. After this ramp, the temperature was periodically changed. An initial temperature(120°C) was given to LCEs, then, it was cooled down to -20°C (cooling rates -3°C/mins) and maintained for about 10 mins. followed by heating up to 120°C and duration about 10mins.

Figure 40 presents the simulated results of the two-way shape memory behavior of monodomain LCEs. The total strain was plotted with curing strain during the repeated cyclic temperature without the external force in figure 40, showing that the repeatable strain according to the cyclic temperature can be explained by the curing strain. Under the UV curing condition, the stored strain occupies much portion of the deformation of the LCEs, and it is converted to curing strain. As the LCE is heated up above T_i, the conformation of the mesogen is changed. Upon heating, the mechanical strain decreases as the randomly distribution of the mesogen increases, i.e., the favorable intermolecular forces acting among mesogens are disrupted and the LCE sample contracts due to entropy elasticity, overall bringing about decreased strain of LCEs. As the LCE is cooled down below T_i, the light induced bond

rearrangement facilitates erasing of birefringence to an isotropic state, which, becomes polydomain [21]. At that time, the curing strain does role of these programmed strain; Stored strain acts as a drive force for the formation of a monodomain of mesogen at low temperatures. This phenomenon continue until the temperature reaches below T_i.

①Programed stated   ②Original state   ③Programed stated   ④ Original stated
 t = 40 s, T = 70 ℃   t = 25 mins, T = 120 ℃   t = 55 mins, T = 70 ℃   t = 75mins, T = 120 ℃
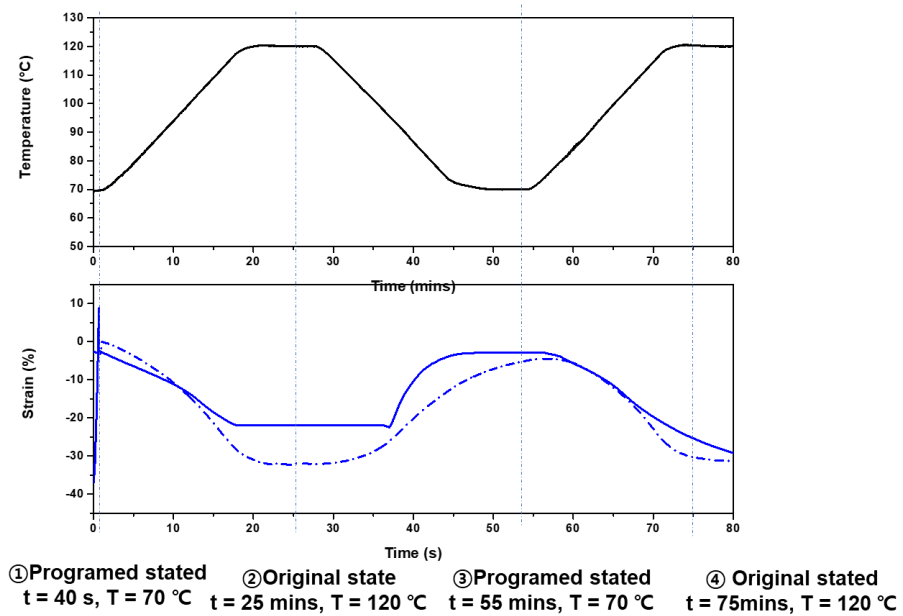
Figure 40 Simulation and experimental result of two-way shape memory behaviors

of polydomain LCEs
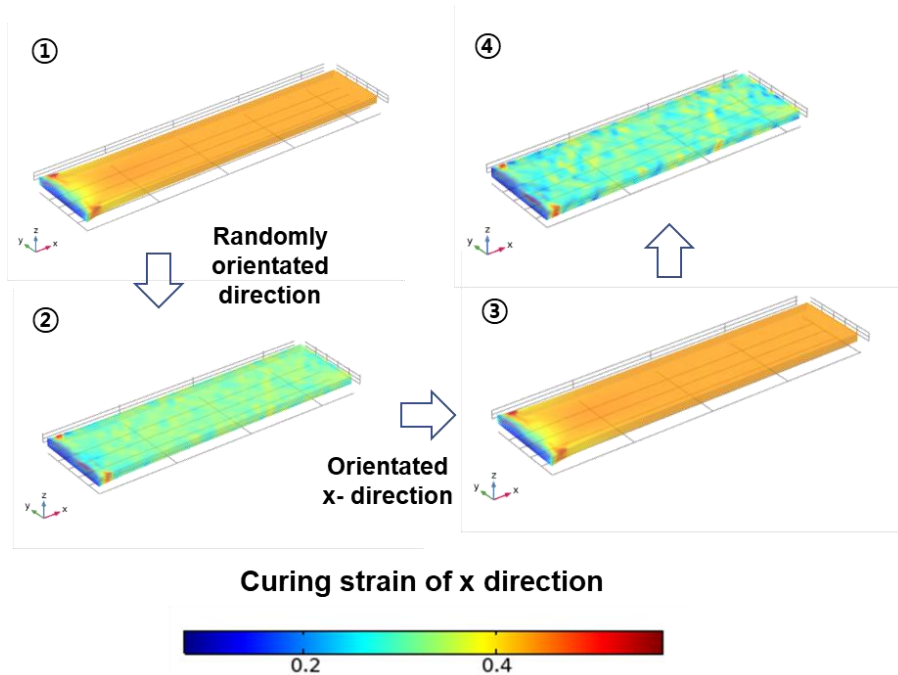
Figure 41 Simulation and experimental result of two-way shape memory behaviors

3.4. Summary

A anisotropic 3D constitutive model was developed to represent the thermomechanical behavior of LCEs. Based on a two-phase (rubbery and glassy phases) isotropic phenomenological model, the direction vector of the mesogen was considered. The orientation of mesogen is newly defined as function of temperature and strain, and the elastic tensor of the mesogen at global coordinate is obtained by tensor transformation method. For polydomain LCEs, Two-way shape memory

behavior of LCEs can be performed at constant stress condition. the applied bias stress drives the formation of a monodomain of liquid crystals when cooling the network below Ti. To describe the two-way behavior of monodomain LCEs, the constitutive model introduces the curing strain concept. Stored strain acts as a drive force for the formation of a monodomain of mesogen. The thermomechanical deformation of a 1D rectangular slab well-simulated by the model, and the model can capture the anisotropic behavior of the mesogen at each state.

4. Concluding remarks

The purpose of this study is to develop 3D constitutive model of rate-dependent and anisotropic shape memory polymers

A temperature-rate dependent 3D constitutive model is developed for SMPs based on a two-phase model consisting of rubbery and glassy phases. Poynting–Thomson model and Arruda-Boyce model are used for the rubbery phase and the glassy phase, respectively. To describe the effect of temperature-rate on SMPs, the volume fraction of each phase is considered from the normalized storage modulus curves obtained under different thermal rate conditions. In addition, the temperature-rate dependent

thermal strain is added to the two-phase model in series. The material parameters of SMPs for the 3D constitutive equation are determined by measuring uniaxial tensile and creep behavior. The constitutive equation is validated by simulating the thermo-mechanical behavior of 1D rectangular slab and a 3D antenna.

Based on the two-phase isotropic rate-dependent model, a new approach constitutive model for LCE was developed considering anisotropic properties of mesogen. The backbone polymer, a component of LCE, was modeled using the two-phase model. Then, the orientation of mesogen according to temperature and external force was defined through the WAXS experiment. Based on the experimental results, the direction vector of mesogen was newly defined as a function of temperature and deformation. It is assumed that the mesogen behaves linearly elastically in the local coordinate, and tensor transformation is used to define the stress according to the temperature and deformation of the mesogen in the global coordinate. For polydomain LCEs, Two-way shape memory behavior of LCEs can be performed at constant stress condition. the applied bias stress drives the formation of a monodomain of liquid crystals when cooling the network below Ti. To describe the two-way behavior of monodomain LCEs, the constitutive model introduces the curing strain concept. Stored strain acts as a drive force for the formation of a monodomain of mesogen. The anisotropic constitutive model is validated by simulating the thermo-mechanical behavior of LCE under various boundary conditions.

Reference

1.   Liu, Y.J., et al., *Shape memory polymers and their composites in aerospace applications: a review.* Smart Materials and Structures, 2014. **23**(2): p. 023001.

2.   Gall, K., et al., *Thermomechanics of the shape memory effect in polymers for biomedical applications.* J Biomed Mater Res A, 2005. **73**(3): p. 339-348.

3.   Zarek, M., et al., *3D Printing of Shape Memory Polymers for Flexible Electronic Devices.* Advanced Materials, 2016. **28**(22): p. 4449-4454.

4.   Behl, M. and A. Lendlein, *Shape-memory polymers.* Materials today, 2007. **10**(4): p. 20-28.

5.   Andrienko, D., *Introduction to liquid crystals.* Journal of Molecular Liquids, 2018. **267**: p. 520-541.

6.   Schuhladen, S., et al., *Iris-Like Tunable Aperture Employing Liquid-Crystal Elastomers.* Advanced Materials, 2014. **26**(42): p. 7247-7251.

7.   Sánchez-Ferrer, A., et al., *Liquid-Crystalline Elastomer Microvalve for Microfluidics.* Advanced Materials, 2011. **23**(39): p. 4526-4530.

8.   Sungur, E., et al., *Temperature tunable optical gratings in nematic elastomer.* Applied Physics A, 2010. **98**(1): p. 119-122.

9.   Sánchez-Ferrer, A., et al., *Photo-Crosslinked Side-Chain Liquid-Crystalline Elastomers for Microsystems.* Macromolecular Chemistry and Physics, 2009. **210**(20): p. 1671-1677.

10.   Yu, Y. and T. Ikeda, *Soft Actuators Based on Liquid-Crystalline Elastomers.* Angewandte Chemie International Edition, 2006. **45**(33): p. 5416-5418.

11.   Liu, C., H. Qin, and P.T. Mather, *Review of progress in shape-memory polymers.* Journal of Materials Chemistry, 2007. **17**(16): p. 1543.

12.   Kularatne, R.S., et al., *Liquid crystal elastomer actuators: Synthesis, alignment, and applications.* Journal of Polymer Science Part B: Polymer Physics, 2017. **55**(5): p. 395-411.

13.   Warner, M. and E.M. Terentjev, *Liquid crystal elastomers*. Vol. 120. 2007: Oxford university press.

14.   White, T.J. and D.J. Broer, *Programmable and adaptive mechanics with liquid crystal polymer networks and elastomers.* Nature Materials, 2015. **14**(11): p. 1087-1098.

15.   Ohm, C., M. Brehmer, and R. Zentel, *Liquid Crystalline Elastomers as Actuators and Sensors.* Advanced Materials, 2010. **22**(31): p. 3366-3387.

16.   Torras, N., et al., *Tactile device based on opto-mechanical actuation of liquid crystal elastomers.* Sensors and Actuators A: Physical, 2014. **208**: p. 104-112.

17.   Yuan, C., et al., *3D printed reversible shape changing soft actuators assisted by liquid crystal elastomers.* Soft Matter, 2017. **13**(33): p. 5558-5568.

18.   Wang, Z., et al., *Reprogrammable, Reprocessible, and Self-Healable Liquid Crystal Elastomer with Exchangeable Disulfide Bonds.* ACS Applied Materials & Interfaces, 2017. **9**(38): p. 33119-33128.

19.	Ambulo, C.P., et al., *Processing advances in liquid crystal elastomers provide a path to biomedical applications.* Journal of Applied Physics, 2020. **128**(14): p. 140901.

20.	Keip, M.-A. and O. Nadgir, *An electro-elastic phase-field model for nematic liquid crystal elastomers based on Landau-de-Gennes theory.* GAMM-Mitteilungen, 2017. **40**(2): p. 102-124.

21.	Mcbride, M.K., et al., *Photoinduced Plasticity in Cross-Linked Liquid Crystalline Networks.* Advanced Materials, 2017. **29**(17): p. 1606509.

22.	Liu, Y., et al., *Thermomechanics of shape memory polymers: uniaxial experiments and constitutive modeling.* International Journal of Plasticity, 2006. **22**(2): p. 279-313.

23.	Tobushi, H., et al., *Thermomechanical constitutive modeling in shape memory polymer of polyurethane series.* Journal of Intelligent Material Systems and Structures, 1997. **8**(8): p. 711-718.

24.	Tobushi, H., et al., *Thermomechanical constitutive model of shape memory polymer.* Mechanics of Materials, 2001. **33**(10): p. 545-554.

25.   Abrahamson, E.R., et al., *Shape memory mechanics of an elastic memory composite resin.* Journal of Intelligent Material Systems and Structures, 2003. **14**(10): p. 623-632.

26.   Diani, J., Y.P. Liu, and K. Gall, *Finite strain 3D thermoviscoelastic constitutive model for shape memory polymers.* Polymer Engineering and Science, 2006. **46**(4): p. 486-492.

27.   Liu, Y.P., et al., *Thermomechanics of shape memory polymers: Uniaxial experiments and constitutive modeling.* International Journal of Plasticity, 2006. **22**(2): p. 279-313.

28.   Lei, M., et al., *Influence of structural relaxation on thermomechanical and shape memory performances of amorphous polymers.* Polymer, 2017. **109**: p. 216-228.

29.   Guo, X.G., et al., *Constitutive model for a stress- and thermal-induced phase transition in a shape memory polymer.* Smart Materials and Structures, 2014. **23**(10): p. 105019.

30.   Chen, Y.C. and D.C. Lagoudas, *A constitutive theory for shape memory polymers. Part I - Large deformations.* Journal of the Mechanics and Physics of Solids, 2008. **56**(5): p. 1752-1765.

31.   Qi, H.J., et al., *Finite deformation thermo-mechanical behavior of thermally induced shape memory polymers.* Journal of the Mechanics and Physics of Solids, 2008. **56**(5): p. 1730-1751.

32.   Park, H., et al., *Three-dimensional constitutive model for shape memory polymers using multiplicative decomposition of the deformation gradient and shape memory strains.* Mechanics of Materials, 2016. **93**: p. 43-62.

33.   Kim, J.H., T.J. Kang, and W.R. Yu, *Thermo-mechanical constitutive modeling of shape memory polyurethanes using a phenomenological approach.* International Journal of Plasticity, 2010. **26**(2): p. 204-218.

34.   Gu, J.P., J.S. Leng, and H.Y. Sun, *A constitutive model for amorphous shape memory polymers based on thermodynamics with internal state variables.* Mechanics of Materials, 2017. **111**: p. 1-14.

35.   Zeng, H., et al., *Modeling the strain rate-, hold time-, and temperature-dependent cyclic behaviors of amorphous shape memory polymers.* Smart Materials and Structures, 2018. **27**(7): p. 075050.

36.   Pan, Z., et al., *A modified phase-based constitutive model for shape memory polymers.* Polymer International, 2018. **67**(12): p. 1677-1683.

37.   Li, Y.X. and Z.S. Liu, *A novel constitutive model of shape memory polymers combining phase transition and viscoelasticity.* Polymer, 2018. **143**: p. 298-308.

38.   Wang, Z.D., et al., *Modeling Thermomechanical Behaviors of Shape Memory Polymer.* Journal of Applied Polymer Science, 2009. **113**(1): p. 651-656.

39.   Li, Y.X., J.Y. Hu, and Z.S. Liu, *A constitutive model of shape memory polymers based on glass transition and the concept of frozen strain release rate.* International Journal of Solids and Structures, 2017. **124**: p. 252-263.

40.   Hong, S.B., et al., *Three-dimensional constitutive model of woven fabric-reinforced shape memory polymer composites considering thermal residual stress.* Smart Materials and Structures, 2019. **28**(3).

41.   Diani, J., et al., *Predicting thermal shape memory of crosslinked polymer networks from linear viscoelasticity.* International Journal of Solids and Structures, 2012. **49**(5): p. 793-799.

42.   Castro, F., et al., *Effects of thermal rates on the thermomechanical behaviors of amorphous shape memory polymers.* Mechanics of Time-Dependent Materials, 2010. **14**(3): p. 219-241.

43.   Biggins, J.S., M. Warner, and K. Bhattacharya, *Elasticity of polydomain liquid crystal elastomers.* Journal of the Mechanics and Physics of Solids, 2012. **60**(4): p. 573-590.

44.   Zhang, Y., et al., *Continuum mechanical modeling of liquid crystal elastomers as dissipative ordered solids.* Journal of the Mechanics and Physics of Solids, 2019. **126**: p. 285-303.

45.   Higaki, H., T. Takigawa, and K. Urayama, *Nonuniform and Uniform Deformations of Stretched Nematic Elastomers.* Macromolecules, 2013. **46**(13): p. 5223-5231.

46.   Tammer, M., et al., *FTIR-Spectroscopy on Segmental Reorientation of a Nematic Elastomer under External Mechanical Fields.* Macromolecular Chemistry and Physics, 2005. **206**(7): p. 709-714.

47.   Fried, E. and S. Sellers, *Orientational order and finite strain in nematic elastomers.* The Journal of Chemical Physics, 2005. **123**(4): p. 044901.

48.   Jiang, Y., L. Jin, and Y. Huo, *Unusual stress and strain concentration behaviors at the circular hole of a large monodomain liquid crystal elastomer sheet.* Journal of the Mechanics and Physics of Solids, 2021. **156**: p. 104615.

49.   Merkel, D.R., et al., *Thermomechanical properties of monodomain nematic main-chain liquid crystal elastomers.* Soft Matter, 2018. **14**(29): p. 6024-6036.

50.   Tokumoto, H., et al., *Probing the in-plane liquid-like behavior of liquid crystal elastomers.* Science Advances, 2021. **7**(25): p. eabe9495.

51.   Anglaret, E., et al., *Molecular Orientation in Liquid Crystal Elastomers.* Macromolecules, 2005. **38**(11): p. 4799-4810.

52.   Mukherjee, P.K., H. Pleiner, and H.R. Brand, *Landau model of the smectic C–isotropic phase transition.* The Journal of Chemical Physics, 2002. **117**(16): p. 7788-7792.

53.   Epp, J., *X-ray diffraction (XRD) techniques for materials characterization*, in *Materials characterization using nondestructive evaluation (NDE) methods*. 2016, Elsevier. p. 81-124.

54.   Hanzon, D.W., et al., *Adaptable liquid crystal elastomers with transesterification-based bond exchange reactions.* Soft Matter, 2018. **14**(6): p. 951-960.

55.   Fried, E. and S. Sellers, *Incompatible strains associated with defects in nematic elastomers.* The Journal of Chemical Physics, 2006. **124**(2): p. 024908.

56.   Keip, M.-A. and K. Bhattacharya, *A phase-field approach for the modeling of nematic liquid crystal elastomers.* PAMM, 2014. **14**(1): p. 577-578.

57.   Oates, W. and H. Wang, *A new approach to modeling liquid crystal elastomers using phase field methods.* Modelling and Simulation in Materials Science and Engineering, 2009. **17**(6): p. 064004.

58.   Conti, S., A. DeSimone, and G. Dolzmann, *Soft elastic response of stretched sheets of nematic elastomers: a numerical study.* Journal of the Mechanics and Physics of Solids, 2002. **50**(7): p. 1431-1451.

59.   Lee, V. and K. Bhattacharya, *Actuation of cylindrical nematic elastomer balloons.* Journal of Applied Physics, 2021. **129**(11): p. 114701.

60.   Leslie, F.M., *Continuum theory for nematic liquid crystals.* Continuum Mechanics and Thermodynamics, 1992. **4**(3): p. 167-175.

61.   Verwey, G.C. and M. Warner, *Compositional Fluctuations and Semisoftness in Nematic Elastomers.* Macromolecules, 1997. **30**(14): p. 4189-4195.

62.   Dey, S., et al., *Soft Elasticity in Main Chain Liquid Crystal Elastomers.* Crystals, 2013. **3**(2): p. 363-390.

9 5

63.   Li, Y., et al., *Three-dimensional thermochromic liquid crystal elastomer structures with reversible shape-morphing and color-changing capabilities for soft robotics.* Soft Matter, 2022. **18**(36): p. 6857-6867.

64.   Joshi, A.A., et al., *Measuring liquid crystal elastic constants with free energy perturbations.* Soft Matter, 2014. **10**(6): p. 882-893.

65.   Petelin, A. and M. Čopič, *Strain dependence of the nematic fluctuation relaxation in liquid-crystal elastomers.* Physical Review E, 2010. **82**(1).

66.   Xu, Y. and Y. Huo, *Continuum modeling of the nonlinear electro-opto-mechanical coupling and solid Fréedericksz transition in dielectric liquid crystal elastomers.* International Journal of Solids and Structures, 2021. **219**: p. 198-212.

67.   Vertogen, G., *The Equations of Motion for Nematics.* Zeitschrift für Naturforschung A, 1983. **38**(12): p. 1273-1275.

68.   Jean-François Sadoc, R.M., Jonathan V. Selinger, *Liquid crystal director fields in three-dimensional non-Euclidean geometries.* New Journal of Physics, 2020. **22**: p. 093036.

69.   He, Q., et al., *Electrically controlled liquid crystal elastomer–based soft tubular actuator with multimodal actuation.* Science Advances. **5**(10): p. eaax5746.

70.   Jiang, Z.C., Y.Y. Xiao, and Y. Zhao, *Shining Light on Liquid Crystal Polymer Networks: Preparing, Reconfiguring, and Driving Soft Actuators.* Advanced Optical Materials, 2019. **7**(16): p. 1900262.

71.   Barnes, M. and R. Verduzco, *Direct shape programming of liquid crystal elastomers.* Soft Matter, 2019. **15**(5): p. 870-879.

72.   Liu, X., S.-K. Kim, and X. Wang, *Thermomechanical liquid crystalline elastomer capillaries with biomimetic peristaltic crawling function.* Journal of Materials Chemistry B, 2016. **4**(45): p. 7293-7302.

73.   Pei, Z., et al., *Mouldable liquid-crystalline elastomer actuators with exchangeable covalent bonds.* Nature Materials, 2014. **13**(1): p. 36-41.

74.   Saed, M.O., et al., *High strain actuation liquid crystal elastomers via modulation of mesophase structure.* Soft Matter, 2017. **13**(41): p. 7537-7547.

75. Maeng, J., et al., *Liquid crystal elastomers as substrates for 3D, robust, implantable electronics.* Journal of Materials Chemistry B, 2020. **8**(29): p. 6286-6295.

76. Kotikian, A., et al., *3D Printing of Liquid Crystal Elastomeric Actuators with Spatially Programed Nematic Order.* Advanced Materials, 2018. **30**(10): p. 1706164.

77. Guin, T., et al., *Layered liquid crystal elastomer actuators.* Nature Communications, 2018. **9**(1).

78. Davidson, E.C., et al., *3D Printable and Reconfigurable Liquid Crystal Elastomers with Light-Induced Shape Memory via Dynamic Bond Exchange.* Advanced Materials, 2020. **32**(1): p. 1905682.

79. Traugutt, N.A., et al., *Liquid-Crystal-Elastomer-Based Dissipative Structures by Digital Light Processing 3D Printing.* Advanced Materials, 2020. **32**(28): p. 2000797.

80. Desimone, A. and G. Dolzmann, *Material instabilities in nematic elastomers.* Physica D: Nonlinear Phenomena, 2000. **136**(1-2): p. 175-191.

81.   Boyce, M.C., D.M. Parks, and A.S. Argon, *Large inelastic deformation of glassy polymers. Part I: rate dependent constitutive model.* Mechanics of materials, 1988. **7**(1): p. 15-33.

82.   Lee, E.H., *Elastic-Plastic Deformation at Finite Strains.* Journal of Applied Mechanics, 1969. **36**(1): p. 1-6.

83.   Lu, S. and K. Pister, *Decomposition of deformation and representation of the free energy function for isotropic thermoelastic solids.* International Journal of Solids and Structures, 1975. **11**(7-8): p. 927-934.

84.   Dudescu, C., et al., *Characterisation of thermal expansion coefficient of anisotropic materials by electronic speckle pattern interferometry.* Strain, 2006. **42**(3): p. 197-205.

85.   An, Y., et al., *Quantitative evaluation of the three-dimensional deployment behavior of a shape memory polymer antenna.* Smart Materials and Structures, 2018. **27**(10): p. 105007.

86.   Gao, J., X. Yang, and L. Huang, *A Numerical Model to Predict the Anisotropy of Polymer Composites Reinforced with High-Aspect-Ratio*

Short Aramid Fibers. Advances in Polymer Technology, 2019. **2019**: p. 1-12.

87.   Kim, J., Y. An, and S. Hong, *MECHANICAL ANALYSIS OF CARBON NANOTUBE/SHAPE MEMORY POLYMER COMPOSITES.* 21st International Conference on Composite Materials, 2017.

Appendix

Appendix A Determination of material parameters of SMPs

Appendix A.1 Rubbery phase

The initial hyperelastic spring constants of the rubbery phase are calculated by assuming that the viscoelastic contribution on the total stretch is negligible at the beginning of the uniaxial tensile test at the strain rate, 0.0016/s [87]. Therefore, the total stretch (λ) is expressed as:

$$\lambda = \lambda_r^e \lambda_r^v \simeq \lambda_r^e = 1 + \varepsilon \tag{A.1}$$

Considering the uniaxial condition, the stress is as follow [1]:

$$\sigma_r = 2C_{10,r}^e[(\lambda_r^e)^2 - (\frac{1}{\lambda_r^e})] + 2C_{01,r}^e[(\lambda_r^e) - (\frac{1}{\lambda_r^e})^2] \tag{A.2}$$

Equation (A.2) can be re-arranged as:

$$\frac{\sigma_r}{2[(\lambda_r^e) - (\frac{1}{\lambda_r^e})^2]} = \lambda_r^e C_{10,r}^e + C_{01,r}^e \tag{A.3}$$

The constants ($C_{10,r}^e$ and $C_{01,r}^e$) are estimated from the polynomial fitting of equation (A.3) within strain range (From 0.4% to 0.8%) (see **Figure A.1**).

The viscoelastic components, viscoelastic spring constants ($C_{10,r}^v$ and $C_{01,r}^v$) and dashpot (κ_r), are determined by a creep test with the initial stress of 0.15 MPa and the creep strain of 1.75% (see **Figure A.2**). According to a Ponynting-Thomson model, the ordinary differential equation governs viscoelastic behavior as follow [32]:

$$\frac{d\lambda_r^v}{dt}[2(\lambda_r^v)^3 + (\frac{1}{\lambda_r^v})^3] = \frac{1}{2}\frac{1}{\kappa_r}[h(C_{10,r}^e, C_{01,r}^e, \lambda_r^e) - h(C_{10,r}^v, C_{01,r}^v, \lambda_r^v)] \tag{A.4}$$

, where

$$h(C_{10,r}^e, C_{01,r}^e, \lambda_r^e) = 2C_{10,r}^e[(\lambda_r^e)^2 - (\frac{1}{\lambda_r^e})] + 2C_{01,r}^e[(\lambda_r^e) - (\frac{1}{\lambda_r^e})^2] \tag{A.5}$$

1 0 2

$$h(C_{10,r}^v, C_{01,r}^v, \lambda_r^v) = 2C_{10,r}^v[(\lambda_r^v)^2 - (\frac{1}{\lambda_r^v})] + 2C_{01,r}^v[(\lambda_r^v) - (\frac{1}{\lambda_r^v})^2] \qquad \textbf{(A.6)}$$

Assuming that the hyperelastic component (equation (A.5)) is dominant in total stretch until the stress becomes a constant value at the stress range of 0 to the initial stress (0.15 MPa), the viscoelastic stretch in equation (A.6) is negligible ($\lambda_r^v \simeq 1$), so equation (A.4) can be rewritten as:

$$\kappa_r = \frac{1}{6} \frac{1}{\dfrac{d\lambda_r^v}{dt}} [h(C_{10,r}^e, C_{01,r}^e, \lambda_r^e)] \qquad \textbf{(A.7)}$$

The dashpot constant (κ_r) can be calculated from equation (A.7).

On the contrary, once the stress maintains constant, it is presumed that the hyperelastic stretch does not change much, hence, λ_r^e is fixed as 1.02. The equation (A.4) is then rearranged as:

$$\frac{[h(C^e_{10,r}, C^e_{01,r}, \lambda^e_r) - 2\kappa_r \frac{d\lambda^v_r}{dt}[2(\lambda^v_r)^3 + (\frac{1}{\lambda^v_r})^3]]}{2(\lambda^v_r + (\frac{1}{\lambda^v_r})^2)} = (\lambda^v_r C^v_{10,r} + C^v_{01,r})$$

(A.8)

The viscoelastic spring constants ($C^v_{10,r}$ and $C^v_{01,r}$) are determined by linear
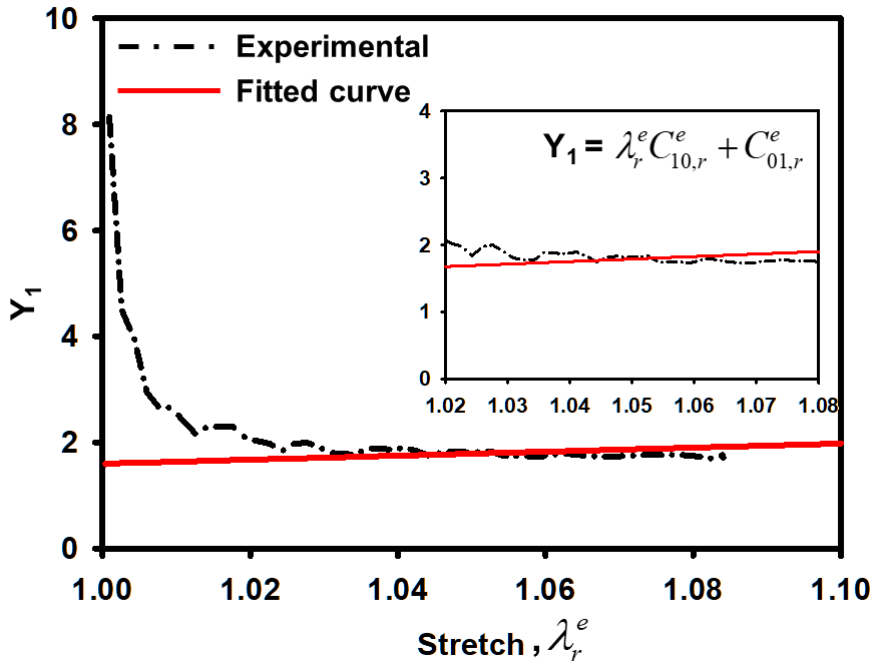
fitting of equation (A.8) (see **Figure A.2**b).

Figure A.1 Determination of hyperelastic spring constants of the rubbery

phase ($C^e_{10,r}$ and $C^e_{01,r}$), where $\mathbf{Y_1} = \sigma_r / [2\{(\lambda^e_r) - (1/\lambda^e_r)^2\}]$. The inset figure
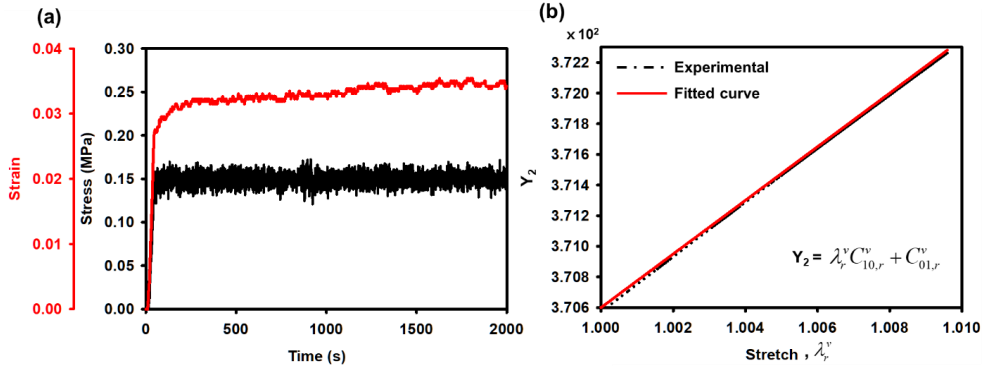
Figure A.2 Creep test for obtaining viscoelastic constants. (a) Stress and strain evolution depending on time. Polynomial fitting to obtain (b) viscoelastic spring constants ($C_{10,r}^v$ and $C_{01,r}^v$). $\mathbf{Y}_2 = \sigma_r /[2\{(\lambda_r^e)-(1/\lambda_r^e)^2\}]$

Appendix A.2 Glassy phase

The material parameters of glassy phase are decided according to the method developed by M. C. Boyce et al. [81]. The stress in the eight-chain spring in the viscoplastic, $\sigma_g^{eight-chain}$, is as follow:

1 0 5

$$\sigma_g^{eight-chain} = \frac{1}{3}C_r\sqrt{N}[(\frac{\lambda_{chain}^p}{\sqrt{N}})\frac{(2.99-1.14(\frac{\lambda_{chain}^p}{\sqrt{N}})^2)}{(1-(\frac{\lambda_{chain}^p}{\sqrt{N}})^2)}]\frac{(\lambda_i^p)^2-\frac{1}{3}I_1}{\lambda_{chain}^p} \qquad \textbf{(A.9)}$$

, where

$$\lambda_{chain}^p = \sqrt{\frac{trace(\mathbf{F}^{vp}\mathbf{F}^{vpT})}{3}} \qquad \textbf{(A.10)}$$

λ_i^p are the principal applied stretches given by the eigenvalues of the viscoplastic stretch tensor.

The stress in viscoplastic dashpot, σ_g^{vp}, is given by the difference between the elastic stress and the stress in the eight-chain as below:

$$\sigma_g^{vp} = \sigma_g^e - \frac{1}{J^e}\mathbf{F}_g^e\sigma_g^{eight-chain}\mathbf{F}_g^e \qquad \textbf{(A.11)}$$

The effective equivalent shear strength, τ, is

$$\tau = \sqrt{\frac{\sigma_{g\ dev}^{vp} : \sigma_{g\ dev}^{vp}}{2}}$$

(A.12)

And the normalized tensor, $\mathbf{N}$, is defined as

$$\mathbf{N} = \frac{\sigma_{g\ dev}^{vp}}{\sqrt{2}\tau}$$

(A.13)

The plastic shear strain rate, $\dot{\gamma}^p$, is given by

$$\dot{\gamma}^p = \dot{\gamma}_0 \exp[-\frac{As}{T}(1-(\frac{\tau}{s})^{5/6})]$$

(A.14)

Considering the flow rule in the Arruda-Boyce theory, the rate of viscoplastic deformation gradient is denoted in the following relation:

$$\frac{d\mathbf{F}_g^{vp}}{dt} = \mathbf{D}^{vp}\mathbf{F}_g^{vp}$$

(A.15)

, where

$$\mathbf{D}^{vp} = \dot{\gamma}^p \, \mathbf{N} \qquad\qquad\qquad \textbf{(A.16)}$$

The rate of athermal shear stress is described as:

$$\dot{s} = h(1 - \frac{s}{s_{ss}}) \dot{\gamma}^p \qquad\qquad\qquad \textbf{(A.17)}$$

, where h is the softening slope given by

$$h \approx \frac{\triangle s}{\triangle \gamma^p} \left(\frac{1}{1 - (s_0 / s_{ss})} \right) \qquad\qquad\qquad \textbf{(A.18)}$$

The shear stress state ratio, s_{ss} / s_0, is determined by comparing the maximum yield stress with the minimum yield stress after softening. The rate of the softening ($\triangle s = s_{ss} - s_0$) with respect to the strain, $\triangle s / \triangle \gamma^p$, is estimated from **Figure A.3**a.

The parameters, $\dot{\gamma}_0$ and A, are determined from experimentally obtained stress-strain curves under different strain rates. The equation (A.14) is rewritten as [81]:

$$\ln(\sqrt{3}\,\dot{\varepsilon}) = B + C(\frac{\sigma_y}{\sqrt{3}s_0})^{5/6} \qquad \textbf{(A.19)}$$

, where

$$B = \ln \dot{\gamma}_0 - \frac{A}{T}s_0 \qquad \textbf{(A.20)}$$

$$C = \frac{A}{T}s_0 \qquad \textbf{(A.21)}$$

$$s_0 = 0.077\frac{E}{2(1-\nu)(1+\nu)} \qquad \textbf{(A.22)}$$

Yield stress, σ_y, and Young's modulus, E are obtained from tensile tests under different strain rates (see **Figure A.3**a). Poisson's ratio, ν, is assumed to be 0.33 and operating temperature, T, is 25°C. The constants, B and C, are determined by linear fitting of equation (A.19) (see **Figure A.3**b). The detailed procedure to obtain material parameters of the glassy phase is represented in **Table 3**.
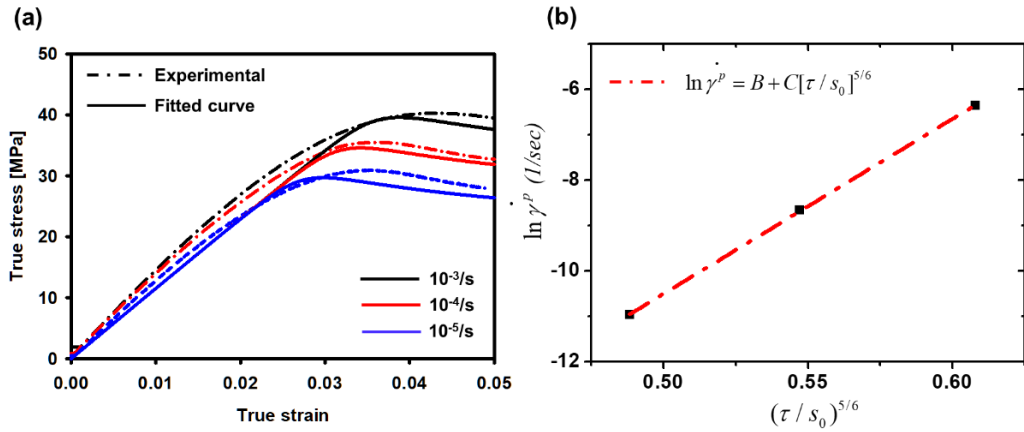
Figure A.3. (a) True stress–strain tensile curves under different strain rate for obtaining material parameters of the glassy phase. (b) Polynomial fitting to obtain strain rate-dependent parameters, $\dot{\gamma}_0$ and A.

Table 3. Step by step procedure to obtain material parameters of the glassy

phase

I. initial condition

1. Assume the viscoplastic deformation gradient ($\mathbf{F}_g^{vp}$) as the identity

tensor ($\mathbf{I}$).

II. Main Calculation

2. Measure Young's modulus (E) from stress-strain curves and

    assume that Poisson's ratio (V) is 0.33.

3. Calculate the elastic stress (σ_e) described by general Hooke's

    law.

4. Calculate the eight-chain stress ($\sigma_{eight-chain}$) using equation (A.9)

    with arbitrary constants, C_r and L.

---

5. Calculate the stress in viscoplastic dashpot (σ_{vp}) using equation (A.11).

6. Calculate the effective equivalent shear strength (τ) using equation (A.12).

7. Check τ. If $\tau > 0$, calculate the normalized tensor ($\mathbf{N}$) using equation (A.13), Else set $\mathbf{N} = 0$.

8. Determine zero stress level activation energy (A) and pre-exponential factor ($\dot{\gamma}_0$) by polynomial fitting of stress-strain curves.

9. Calculate the plastic shear strain rate ($\dot{\gamma}^p$) using equation (A.14).

10. Update $\mathbf{F}_g^{vp}$ using equation (A.15).

11. Measure softening slope (h) and shear stress state ratio (s_{ss}/s_0)from stress-strain curves (equation A.18).

12. Update the athermal shear stress (s) using equation (A.17), then

   go to step 3.

III. Iteration procedure

13. Repeat from step 3 to12 with different arbitrary constants (C_r and

L), until the RMS error between experimental and simulated curves is

less than 1%.

Appendix B Wide Angle X-Ray Scattering to observe the orientation of the mesogen

Wide-angle X-ray scattering (WAXS) measurements were performed using a Xeuss2.0 instrument to quantify the degree of orientation of mesogens in LCEs at various temperature. The instrument was equipped with a reversed-biased silicon diode array sensor. The wavelength of radiation (λ) was 1.54189 Å and the sample to detector distance was 70mm. The scattering patterns were collected with 487 x 619 pixels (pixel size: 172 x 172μm^2).

The orientation of the mesogens can be analyzed by azimuthal intensity

distribution of the mesogen direction (Figure B.1). Using Full Width Half Maximum (FWHM), we could quantify the degree of orientation as a function of temperature and strain. As shown in the Figure B.1, the width corresponding to the one-half maximum intensity value is the value of the FWHM, and the more aligned mesogen molecules, the smaller the width of the FWHM.
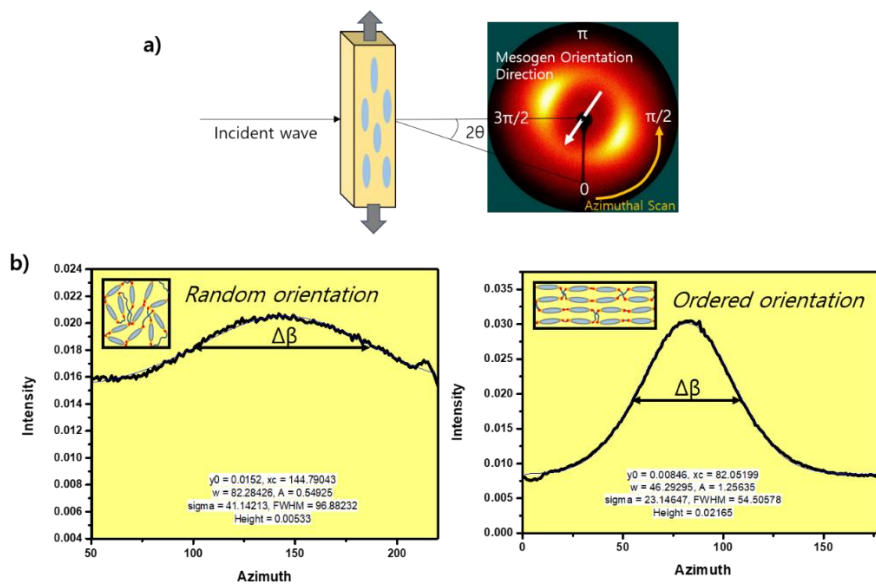

Figure B.1. WAXS method used for determining the molecular orientation. X-ray scattering pattern obtained the molecules direction. (a)The orientation of the mesogens can be analyzed by azimuthal intensity distribution of the mesogen direction. (b) Azimuthal intensity profiles of WAXS. $\Delta\beta$ is the FWHM of the distribution.

Korean abstract

형상기억고분자는 온도, 전기, 빛, 습도 등의 외부 자극에 따라 변형된 형상에서 본래의 형태로 형상을 기억하는 스마트 고분자의 한 종류이다. 또한 형상기억고분자에 액정메소젠을 첨가하면 변형방향에 따라 고분자의 새로운 특성이 발현되고, 이를 액정엘라스토머라고 한다. 액정엘라스토머의 중요한 특징 중 하나는 외부 힘과 온도에 따라 액정메소젠의 방향이 변화한다는 것이다. 이러한 특성을 사용하여 정렬된 액정엘라스토머는 상전이를 통해 외부 응력이 낮거나 없는 상태에서 형상을 가역적으로 변경할 수 있다. 형상기억고분자 및 액정엘라스토머를 사용하는 장치의 성공적인 설계를 위해 다양한 조건에서 형상기억고분자 및 액정엘라스토머의 형상 기억 및 기계적성질을 예측하는 조성방정식 모델이 연구되고 있다. 따라서 본 연구에서는 고무상과 유리상으로 구성된 2상 모델을 기반으로 형상기억고분자 및 액정엘라스토머에 대한 온도 속도 의존 및 이방성을 고려한 3차원 조성방정식 모델을 개발하였다.

형상기억고분자에 대한 온도 속도의 영향을 설명하기 위해 온도에 따라 달라지는 각 상의 부피 분율의 변화를 다른 온도 속도조건에서 고려하였다. 또한 온도 속도에 따른 열 변형을 모델링하여 조성방정식에 반영하였다. Poynting–Thomson 모델과 Arruda–Boyce 모델은 고온에서의

거동 그리고 저온에서의 거동을 설명하기 위하여 사용되었다. 3차원 구성 방정식에 대한 SMP의 재료 매개변수는 단축 인장 및 크리프 거동을 측정하여 결정하였다. 개발된 조성방정식은 1D 직사각형 슬래브와 3D 안테나의 온도변화에 따른 변형을 시뮬레이션하여 검증하였다.

액정엘라스토머의 열역학적 모델링 및 시뮬레이션은 메조겐의 온도의 영향뿐만 아니라 방향에 따른 이방성성질을 고려해야한다. 본 연구에서는 등방성 2상 모델을 기반으로 메조겐의 이방성 특성을 고려하여 액정엘라스토머의 새로운 조성방정식 모델을 개발하였다. 액정엘라스토머의 구성요소인 백본 폴리머는 등방성 2상 모델을 사용하여 모델링 하였다. 그리고 실험을 통해 온도와 외력에 따른 메소젠의 방향성을 정의하였다. 실험 결과를 바탕으로 메조겐의 방향 벡터를 온도와 변형의 함수로 새롭게 정의하였다. 메조겐은 국부 좌표에서 선형탄성적으로 거동하는 것으로 가정하고, 텐서변환을 활용하여 전역 좌표에서 메조겐의 온도 및 변형에 따른 응력을 새롭게 정의하였다. 마지막으로, 방향성이 정의된 액정엘라스토머의 가역적 변형을 정의 하기 위하여 경화변형률이라는 개념을 새롭게 정의하였다. 본 연구에서 이방성을 고려한 액정엘라스토머의 조성방정식 모델은 다양한 경계 조건에서 변형거동을 시뮬레이션하여 검증하였다.